Acta Materialia 268 (2024) 119747

Contents lists available at ScienceDirect

Acta Materialia

journal homepage: www.elsevier.com/locate/actamat

Thermodynamic modeling of Fe-Nb and Fe-Nb-Ni systems supported by first-principles calculations and diffusion-multiple measurements

Hui Sun [a,*], Chuangye Wang [b], Shun-Li Shang [a], Allison M. Beese [a,c], Ji-Cheng Zhao [b], Zi-Kui Liu [a]

[a] Department of Materials Science and Engineering, Pennsylvania State University, University Park, PA 16802, USA
[b] Department of Materials Science and Engineering, University of Maryland, College Park, MD 20742, USA
[c] Department of Mechanical Engineering, Pennsylvania State University, University Park, PA 16802, USA

ARTICLE INFO

Keywords:
CALPHAD modeling
Fe-Nb
Fe-Nb-Ni
EPMA
WDS
First-principles and phonon calculations
TCP phases

ABSTRACT

The Fe-Nb and Fe-Nb-Ni systems are remodeled using updated sublattice models for the topologically close-packed (TCP) phases of Laves_C14, δ and μ with new experimental data and first-principles and phonon calculations based on density functional theory (DFT). Scanning electron microscopy (SEM) imaging, electron probe micro-analyzer (EPMA), and wavelength-dispersive spectroscopy (WDS) are used to determine phase compositions and tie-lines in the Fe-Nb-Ni system through a diffusion multiple isothermally treated at 1373 K. The three-, three-, and five- sublattice models are used for Laves_C14, δ, and μ phases according to their Wyckoff positions, respectively. DFT calculations are employed to predict thermochemical data as a function of temperature for Laves_C14, δ, and μ phases. The new thermodynamic description of the Fe-Nb-Ni system includes a new hexagonal phase named - hP24 - and the updates for the Fe-Nb system and reproduces better the experimental and computational thermochemical and phase equilibrium data from the present study and the literature. The new results will improve thermodynamic predictions of TCP and other phases in both Fe-based and Ni-based alloy systems.

1. Introduction

Topologically close-packed (TCP) phases, also known as Frank-Kasper phases [1], refer to a group of intermetallic compounds with complex crystalline structures and high coordination numbers. These phases are commonly observed in metallic alloys, including Ni-based superalloys [2], Co-based superalloys [3], and high-entropy alloys [4]. The formation of TCP phases can lead to the depletion of refractory elements from the matrix, resulting in a reduction of solid solution strengthening in the matrix such as FCC-based γ phase in Ni-based superalloys [2]. Furthermore, TCP phases are often brittle and hence detrimental to mechanical properties of alloys; for instance, the Laves_C14 phase (termed as C14 in the present study) in P92 steel reduces the Charpy toughness to 25% of the as-received samples after 3000 h of ageing [5]. Similarly, the formation of μ-Nb_7Ni_6 after 100 h of ageing decreases ~150 MPa in yield strength in a Ni-based superalloy [6]. After stress relief heat treatment, the formation of approximately 10 vol.% of δ-$NbNi_3$ was found to cause a 45% decrease in the fracture strain in Inconel 625 [7]. Therefore, TCP phases play a crucial role in determining mechanical properties of relevant alloys. Hence, to design and develop advanced materials with optimized properties for applications, it is important to have a better understanding and prediction of the formation of TCP phases.

This study focuses on thermodynamic properties and phase equilibria of the TCP phases in the Fe-Nb-Ni system, which includes the C14 phase $P6_3/mmc$ (No. 194), the δ phase with space group *Pmmn* (No. 59) [8], and the μ phase with space group $R\bar{3}m$ (No. 166) [9]. Our study includes diffusion multiple experiments, first-principles calculations based on density functional theory (DFT) [10] and machine learning (ML), as well as CALPHAD thermodynamic modeling. There are three Wyckoff sites (2a, 6h, and 4f) with space group $P6_3/mmc$ (No. 194) in C14, three Wyckoff sites in δ, and five Wyckoff sites in μ, as shown in Table 1. A complete description of these phases thus requires the three-, three-, and five-sublattice models, respectively, while models with fewer sublattices have been used in previous publications such as a two-sublattice model for μ plus an arbitrary value of 5000 J/mol-atom assigned to enthalpy of formation ($\Delta_f H$) for a number of endmembers with one element in each sublattice [11]. Furthermore, new experimental data have been published for the Fe-Nb and Fe-Nb-Ni systems after the latest CALPHAD modeling study by Mathon et al. [11],

* Corresponding author.
E-mail address: suh960@psu.edu (H. Sun).

https://doi.org/10.1016/j.actamat.2024.119747
Received 13 October 2023; Received in revised form 18 January 2024; Accepted 6 February 2024
Available online 8 February 2024

Table 1
Wyckoff positions of the C14, δ-$NbNi_3$ and μ-Nb_7Ni_6 phases in coordination x, y, z.

Wyckoff positions of C14 [a]	x	y	z
2a	0	0	0
6h	0.830	0.660	0.25
4f	0.667	0.333	0.933
Wyckoff positions of δ [b]	x	y	z
2a	0	0	0.318
2b	0	0.5	0.651
4f	0.75	0	0.841
Wyckoff positions of μ [c]			
3a	0	0	0
6c (1)	0	0	0.167
6c (2)	0	0	0.346
6c (3)	0	0	0.448
18h	0.5	0.5	0.590

[a] C14 with space group $P6_3/mmc$ (no. 194), Pearson symbol hp12, Strukturbericht designation C14, and prototype of $MgZn_2$ [117].
[b] δ with space group Pmmn (no. 59), Pearson symbol oP8, Strukturbericht designation $D0_a$, and prototype of β-Cu_3Ti [8].
[c] μ with space group $R\bar{3}m$ (no. 166), Pearson symbol hR13, Strukturbericht designation $D8_5$, and prototype of Fe_7W_6 [9].

requiring remodeling of the Fe-Nb and Fe-Nb-Ni systems. In the current study, both the binary and ternary systems are remodeled using the sublattice models based on Wyckoff sites of the TCP phases and data acquired in the present study including experimental phase equilibria measurements in the Fe-Nb-Ni system at 1373 K and enthalpies of formation of all endmembers predicted by DFT-based first-principles calculations.

2. Overview of previous CALPHAD modeling

2.1. Previous CALPHAD modeling of Fe-Nb

The Fe-Nb binary system contains two TCP phases (C14 and μ) and three solution phases (BCC_A2, FCC_A1, and liquid). Several thermodynamic descriptions have been developed for Fe-Nb [11–20] with the sublattice models summarized in Table 2. Coelho et al. [14] and Srikanth and Petric [15] treated μ as a stoichiometric compound without considering the composition range in μ as measured by Voβ et al. [21] and Zelaya et al. [22,23]. Huang et al. [12] and Lee et al. [13] described μ with a narrower solubility than that in experimental data by Zelaya et al. [22,23]. Toffolon and Servant [19] used a two-sublattice model $(Fe,Nb)_2(Fe,Nb)_1$ for C14 and three-sublattice $((Fe)_{18}(Nb)_{18}(Fe,Nb)_3)$ and four-sublattice $((Fe,Nb)_1(Fe,Nb)_2(Fe)_6(Nb)_4)$ models for μ. Mathon et al. [11] used $(Fe,Nb)_1(Fe,Nb)_2$ for C14 and $(Nb)_6(Fe,Nb)_7$ for μ in order to reduce model parameters in the Fe-Nb-Ni system. Liu et al. [16] used $(Fe,Nb)_1(Fe,Nb)_2$ for C14 and $(Fe,Nb)_1(Nb)_4(Fe,Nb)_2(Fe,Nb)_6$ for μ and employed DFT-based calculations to predict their enthalpies of formation.

Table 2
Sublattice models for both C14 and m (Fe7Nb6) used in previous CALPHAD modeling studies.

References	Models for Laves_C14	Models for m
Huang et al. [12]	$(Fe)_2(Nb)_1$	$(Fe)_7(Nb)_2(Fe,Nb)_4$
Lee et al. [13]	$(Fe,Nb)_2(Fe,Nb)_1$	$(Fe)_7(Nb)_2(Fe,Nb)_4$
Coelho et al. [14]	$(Fe)_2(Nb)_1$	$(Fe)_7(Nb)_6$
Srikanth and Petric [15]	$(Fe)_6(Fe,Nb)_2(Fe,Nb)_4$	$(Fe)_{21}(Nb)_{19}$
Toffolon and Servant [19]	$(Fe,Nb)_2(Fe,Nb)_1$	$(Fe)_{18}(Nb)_{18}(Fe,Nb)_3$ $(Fe,Nb)_1(Fe,Nb)_2(Fe)_6(Nb)_4$
Mathon et al. [11]	$(Fe,Nb)_2(Fe,Nb)_1$	$(Nb)_6(Fe,Nb)_7$
Liu et al. [16]	$(Fe,Nb)_2(Fe,Nb)_1$	$(Fe,Nb)_1(Nb)_4(Fe,Nb)_2(Fe,Nb)_6$
Khvan and Hallstedt [17]	$(Fe,Nb)_2(Fe,Nb)_1$	$(Fe,Nb)_1(Nb)_4(Fe,Nb)_2(Fe,Nb)_6$
He et al. [18]	$(Fe,Nb)_2(Fe,Nb)_1$	$(Fe,Nb)_1(Nb)_4(Fe,Nb)_2(Fe,Nb)_6$
Pan et al. [20]	$(Fe,Nb)_2(Fe,Nb)_1$	$(Fe,Nb)_2(Fe,Nb)_4$ $(Fe,Nb)_7$

In modeling the Fe-Mn-Nb-C system, Khvan and Hallstedt [17] revised the Fe-Nb system by Liu et al. [16], to reproduce the experimentally determined activity of Nb in the austenite at low temperatures. He et al. [18] used the same model by Liu et al. [16] and revised the model parameters to improve the agreement of the Nb solubility in C14 in the Fe-Al-Nb system with experimental phase boundaries by Voβ et al. [21]. Pan et al. [20] remodel Fe-Nb based on the heat capacity of C14 and μ measured by Silva et al. [24]. However, Pan et al. [20] used the sublattice models of $(Fe,Nb)_7(Fe,Nb)_4(Fe,Nb)_2$ for μ and $(Fe,Nb)_1(Fe,Nb)_2$ for C14, which cannot fully describe the atomic behavior in 5 Wyckoff positions.

It is clear that the simplified sublattice models used in the literature cannot reproduce site occupancy in TCP phases such as those of Nb in the μ-Nb_7Ni_6 phase in the Nb-Ni system [25]. Additionally, experimental data from Silva et al. [24] were published after previous modeling studies [11–19]. In the present study, the Fe-Nb system is remodeled with the three-sublattice model $(Fe,Nb)_1(Fe,Nb)_2(Fe,Nb)_3$ for C14 and the five-sublattice model $(Fe,Nb)_1(Fe,Nb)_2$-$(Fe,Nb)_2(Fe,Nb)_2(Fe,Nb)_6$ for μ, based on their Wyckoff positions as shown in Table 1. The complete sublattice model can provide accurate description of atomic behavior in each Wyckoff positions and offer more reliable predictions of TCP phase formation.

2.2. Previous CALPHAD modeling of Fe-Ni and Nb-Ni

The Fe-Ni system was widely studied [26–35]. There are five stable phases in Fe-Ni, - liquid, FCC_A1, BCC_A2, FCC_$L1_2$, and FCC_$L1_0$. The modeling parameters by Ohnuma et al. [35] as shown in Fig. S1 (a) are adopted in the present study due to their capability to account for experimental results at temperatures above 673 K and both chemical and magnetic ordering. Since Ohnuma et al. [35] adopted Xiong's magetic parameters (T_C and $\bar{\beta}$) for pure Ni in BCC_A2 and FCC_A1 phase, with slight modifications made to incorporate magnetic parameters from the Scientific Group Thermodata Europe (SGTE) [36]. As a result, this study can be integrated with other ongoing studies that utilize the same magnetic parameters from SGTE. In their study, FCC_A1, FCC_$L1_2$, and FCC_$L1_0$ are modeled with the same Gibbs energy model as the latter two are the ordered solution phases of FCC_A1.

The Nb-Ni system comprises six phases, - three solution phases (FCC_A1, BCC_A2, and liquid) and three intermetallic compounds (μ, δ, and $NbNi_8$). The Nb-Ni system was modeled six times using the CALPHAD approach [37–42] and was recently remodeled by the some of the present authors [25] as shown in Fig. S1 (b) which was employed in the present study since it used sublattice models based on Wyckoff positions for the TCP phases, i.e., five-sublattice $(Nb,Ni)_1(Nb,Ni)_2(Nb,Ni)_2$ $(Nb,Ni)_2(Nb,Ni)_6$ for μ and three sublattice $(Nb,Ni)_1(Nb,Ni)_1(Nb,Ni)_2$ for δ, with a better description of phase diagram and thermochemical data.

2.3. Previous CALPHAD modeling of Fe-Nb-Ni

The Fe-Nb-Ni ternary system contains ten phases, i.e., liquid, BCC_A2, FCC_A1, C14, FCC_$L1_2$, FCC_$L1_0$, hP24 (see its definition below), μ, δ, and $NbNi_8$. Mathon et al. [11] modeled the Fe-Nb-Ni system with a two-sublattice model for δ: $(Fe,Nb,Ni)_1(Fe,Nb,Ni)_3$, a two-sublattice model for C14: $(Fe,Nb,Ni)_1(Fe,Nb,Ni)_2$, and a two-sublattice model for μ: $(Nb)_6(Fe,Nb,Ni)_7$; as shown in Table 3. Mathon et al. [11] did not include the hexagonal A_3B-type phase with Pearson symbol of hP24 (termed as the hP24 phase hereafter) reported by Takeyama et al. [43], which was further treated by Hasebe et al. [44] as a stoichiometric phase. The solubility range of Fe in C14 at 1473 K from the model by Mathon et al. [11] is 35.4 to 100.0 at. % Fe which

Table 3
Sublattice models used by the present modeling work, Pan et al. [20], and Mathon et al. [11].

Phases	This model	Mathon et al. [11]	Pan et al. [20]
BCC_A2	$(Fe,Nb,Ni)_1(Va)_3$	$(Fe,Nb,Ni)_1(Va)_3$	$(Fe,Nb)_1(Va)_3$
δ	$(Fe,Nb,Ni)_1(Fe,Nb,Ni)_1$ $(Fe,Nb,Ni)_2$	$(Fe,Nb,Ni)_1(Fe,Nb,Ni)_3$	
FCC_A1	$(Fe,Nb,Ni)_1(Va)_1$	$(Fe,Nb,Ni)_1(Va)_1$	$(Fe,Nb)_1(Va)_1$
FCC_L1_2	$(Fe,Nb,Ni)_1(Fe,Nb,Ni)_1$ $(Fe,Nb,Ni)_1(Fe,Nb,Ni)_1$ $(Va)_4$	$(Fe,Nb,Ni)_3(Fe,Nb,$ $Ni)_1(Va)_4$	
FCC_L1_0	$(Fe,Nb,Ni)_1(Fe,Nb,Ni)_1$ $(Fe,Nb,Ni)_1(Fe,Nb,$ $Ni)_1(Va)_4$		
C14	$(Fe,Nb,Ni)_1(Fe,Nb,Ni)_2$ $(Fe,Nb,Ni)_3$	$(Fe,Nb,Ni)_1(Fe,Nb,Ni)_2$	$(Fe,Nb)_1(Fe,$ $Nb)_2$
liquid	$(Fe,Nb,Ni)_1$	$(Fe,Nb,Ni)_1$	$(Fe,Nb)_1$
μ	$(Fe,Nb,Ni)_1(Fe,Nb,Ni)_2$ $(Fe,Nb,Ni)_2(Fe,Nb,Ni)_2$ $(Fe,Nb,Ni)_6$	$(Nb)_6(Fe,Nb,Ni)_7$	$(Fe,Nb)_2$ $(Fe,Nb)_4(Fe,$ $Nb)_7$
$NbNi_8$	$(Nb)_1(Ni)_8$		

disagrees with the 30.0 to 100.0 at. % Fe reported by Takeyama et al. [43]. As shown in Section 2.1, the phase boundaries around μ calculated from the database by Mathon et al. [11] disagree with experimental data from this work. In the present study, a five-sublattice model for μ and three-sublattice models for C14 and δ are used to remodel the ternary Fe-Nb-Ni system together with the three binary systems discussed above. Hasebe et al. [44] also modeled the Fe-Nb-Ni system with a two-sublattice model for δ: $(Fe,Nb,Ni)_1(Fe,Nb,Ni)_3$, a two-sublattice model for C14: $(Fe,Nb,Ni)_1(Fe,Nb,Ni)_2$, and a two-sublattice model for μ: $(Nb)_6(Fe,Nb,Ni)_7$, and also $(Fe)_{0.246}(Nb)_{0.216}(Ni)_{0.538}$ for hP24 phase. However, the parameters are not provided in Hasebe et al. [44]. Therefore, comparions are only done with the modeling by Mathon et al. [11] in section 5.5.

3. Current status of thermochemical and phase equilibrium data

3.1. Thermochemical data of Fe-Nb

The values of $\Delta_f H$ in the Fe-Nb system were measured by four groups [45–48]: Meschel et al. [44] using direct reaction calorimetry, Syutkin et al. [48] using drop solution calorimetry, Drobyshev et al. [46] using electromotive force (EMF) at 1224 – 1393 K, and Barbi et al. [47] using EMF at 1000 – 1400 K. However, large differences (around 15 kJ/mol-atom) were found among the measurements as shown in Fig. 1.

To investigate the measured $\Delta_f H$ from different methods, $\Delta_f H$ values of six compounds (including Fe_2Ta, Fe_3Y, Fe_2Y, Fe_2Nb, Co_2Nb, and Nb_3Ni) are collected in Fig. 2 from direct reaction calorimetry by Meschel et al. [45], drop solution calorimetry [48], EMF [46,49–55], and DFT values from OQMD [56] and Materials Project (MP) [57]. Fig. 2 shows that the $\Delta_f H$ values of six compounds by Meschel et al. [45] are systematically less negative than those from the drop solution calorimetry [48], EMF [49–55], and DFT, likely due to the incompletely reaction of the samples in the measurements by direct reaction calorimetry [45]. For Nb-containing compounds (Fe_2Nb, Co_2Nb, and Nb_3Ni), $\Delta_f H$ from EMF [46,52–55] is lower than both the values from DFT. This is because EMF used NbO as the measured electrode, resulting in large errors in evaluating the chemical potential of Nb from possible NbO. Therefore, the values from both DFT and experimental data by Syutkin et al. [48] were employed in the present study.

There are three sets of experiments on the enthalpy of mixing of liquid at the Fe-rich region of the Fe-Nb system [58,59] as shown in Fig. 3 (a). Iguchi et al. [58] measured the enthalpy of mixing of liquid at 1873K using the isoperibol calorimeter method, showing values of 0 to -9.60 kJ/mol-atom from 0 to 25.0 at. % Nb. Sudavtsova et al. [59] measured the enthalpy of mixing of liquid at 1960 K through the calorimeter method with values of 0 to -10.60 kJ/mol-atom from 0 to 20.0

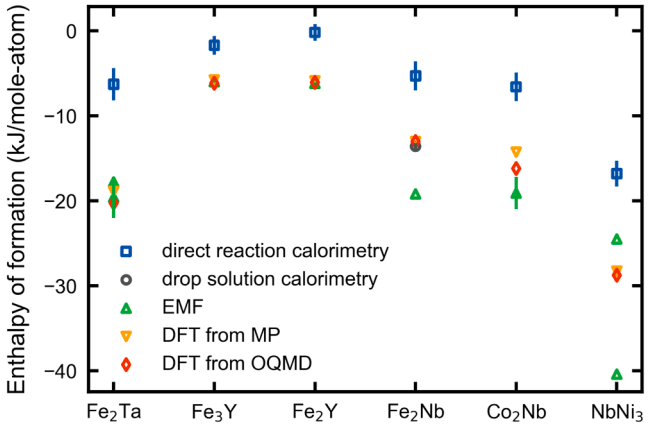

Fig. 2. Enthalpy of formation ($\Delta_f H$) of six compounds (Fe_2Ta, Fe_3Y, Fe_2Y, Fe_2Nb, Co_2Nb, and Nb_3Ni) from direct reaction calorimetry from Meschel et al. [45], drop solution calorimetry [48], EMF [45,48–54], and DFT values from both OQMD [56], and the Materials Project (MP) [57].

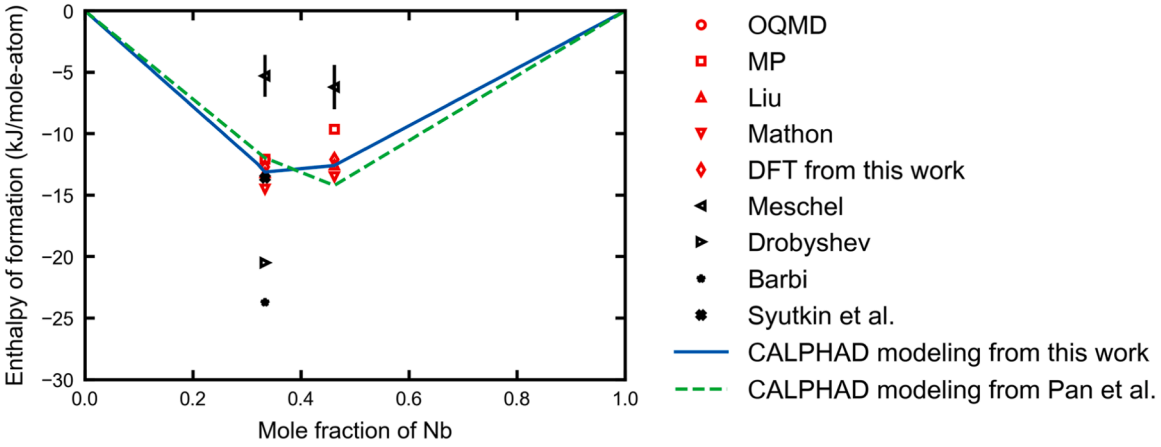

Fig. 1. Predicted values of enthalpy of formation ($\Delta_f H$) of the Fe-Nb system from DFT-based calculations OQMD [56], the Materials Project (MP) [57], Liu et al. [16], Mathon et al. [11] at 0 K and CALPHAD modeling at 298 K from the present study (blue solid line), and results from Pan et al. [20] (green dash line) in comparison with experimental data by Syutkin et al. [48], Meschel et al. [45], Drobyshev et al. [46] and Barbi et al. [47]. (For interpretation of the references to colour in this figure legend, the reader is referred to the web version of this article.)

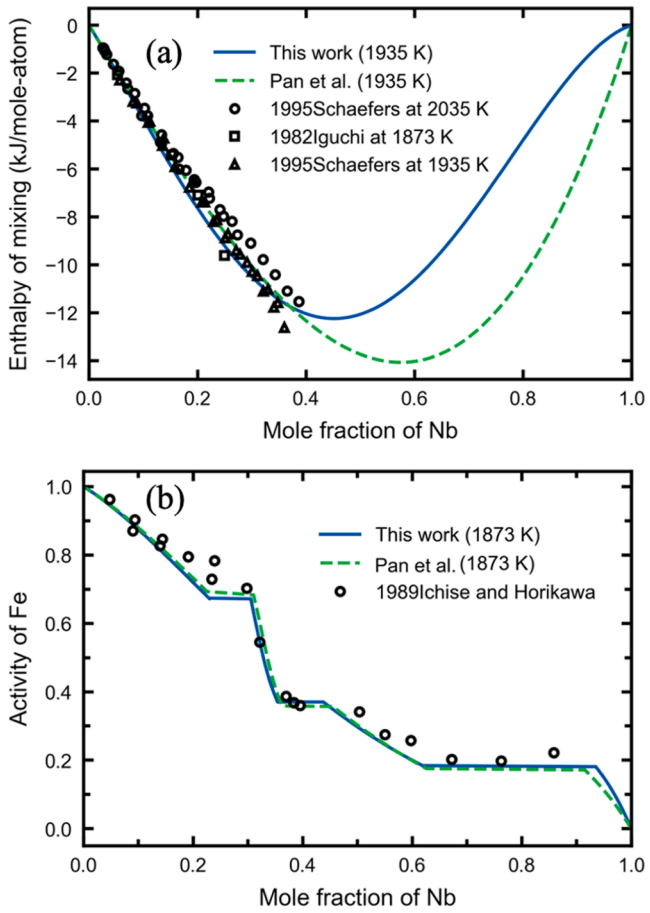

Fig. 3. (a) ΔH_{mix} values of liquid at 1935 K from the present study and Pan et al.'s CALPHAD modeling [20] in comparison with experiments data by Iguchi et al. [58] at 1873 K, and by Schaefers et al. [60] at 1935 K and 2035 K. (b) Activity values of Fe at 1873 K from the present study and Pan et al.'s CALPHAD modeling [20] in comparison with experiments data by Ichise and Horikawa [58].

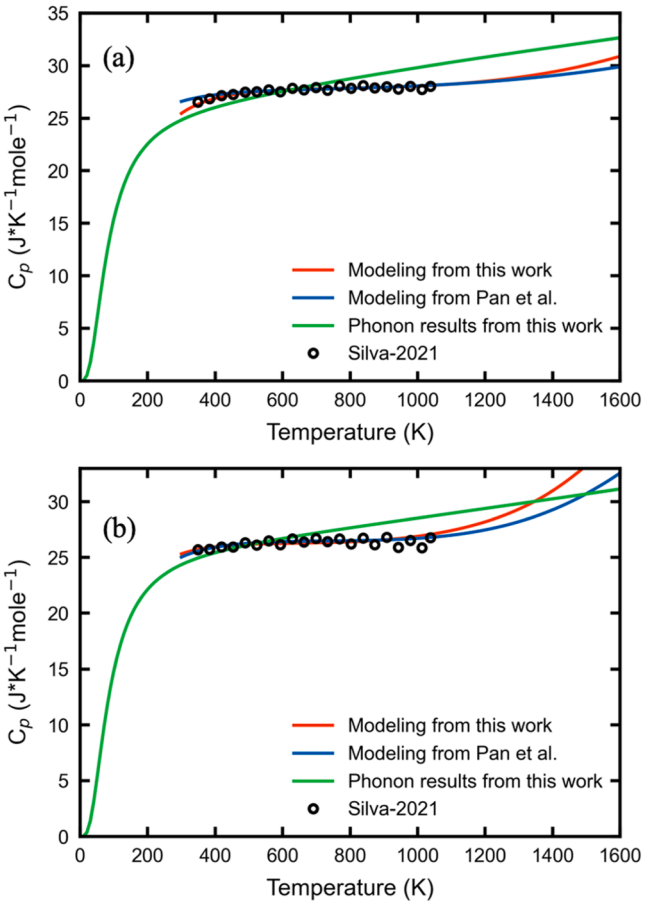

Fig. 4. Heat capacity values of (a) Laves_C14 and (b) μ from both the present study (red line) and that by Pan et al.'s CALPHAD modeling [20] (blue line) with experimental data from Silva et al. [24] and phonon results of C14_$Fe_1Nb_2Fe_3$ and μ_$Nb_6Nb_6Nb_6Fe_{18}Fe_3$ endmembers from this study (green line). (For interpretation of the references to colour in this figure legend, the reader is referred to the web version of this article.)

at. % Nb. Schaefers et al. [60] determined the enthalpy of mixing of liquid at 1935 K and 2035 K by the levitation alloying calorimetry, showing values of 0 to -11.53 kJ/mol-atom from 0 to 38.6 at. % Nb. The results from Iguchi et al. [58] and Schaefers et al. [59] are in agreement with each other, with a difference less than 2 kJ/mol-atom. However, the value from Sudavtsova et al. [59] shows a large deviation (4 kJ/mol-atom) at 20 at. % Nb. Therefore, the data obtained by Iguchi et al. [58] and Schaefers et al. [60] are employed in the present assessment.

The activity of Fe in Fe-Nb was measured by Ichise and Horikawa [58] at 1873 K using the Knudsen cell mass spectrometry, as shown in Fig. 3 (b). This result is included in the present study. Heat capacities of C14 and μ were measured by Silva et al. [24] using the differential scanning calorimetry (DSC) as presented in Fig. 4, which are also used in the present CALPHAD modeling.

3.2. Phase equilibrium data in Fe-Nb

Paul and Swartzendruber [61] presented a critical review of experimental data of the Fe-Nb system with two intermetallic phases (C14 and μ) [62–70]. Zelaya et al. [22,23] further studied the system using optical microscope (OM), X-ray diffraction (XRD), differential thermal analysis (DTA), and electron probe microanalysis (EPMA) and observed a narrower composition range of C14 (32 – 37 at. % Nb at around 1673-1773 K) and a higher melting temperature (1793 K) for μ than those reviewed by Paul and Swartzendruber [61]. The homogeneity ranges of C14 and μ were investigated by Gruner et al. [71] at 1373 K and Takeyama et al. [43] at 1473 K using EPMA. Voβ et al. [21] measured the homogeneity ranges and the invariant reactions in Fe-Nb using OM, EMPA, and DTA. All the invariant reactions are summarized in Table 4 and plotted in Fig. 5. (a), and all the experimental data presented above are considered in the present modeling.

3.3. Phase equilibrium data in Fe-Nb-Ni in the literature

Peard and Borland et al. [72] observed the formation of both δ and C14 at 1048 K in a 56.4Fe-3.8Nb-39.8Ni sample (at. % and the same thereafter). Leitch and Chaturvedi [73] reported the compositions of FCC_A1 as 68.5Fe-2.1Nb-29.4Ni at 1523 K and 70.3Fe-0.6Nb-29.1Ni at 1073 K when it is in equilibrium with C14. Manenc et al. [74], Kirman [75], Manenc [76], and Quist et al. [77] reported a $D0_{22}$ phase. However, this phase was not observed by Hasebe et al. [44], and is thus not considered in the present modeling.

Panteleimonov and Aleshina [78] reported a three-phase equilibrium between liquid (6.2Fe-27.0Nb-56.8Ni), C14 (38.8Fe-29.8Nb-31.4Ni), and δ (5.1Fe-25.6Nb-69.3Ni)) at 1563 K by XRD, Scanning electron microscopy (SEM), and DTA. Varli et al. [79] observed a continuous μ phase across the ternary from Fe_7Nb_6 to Nb_6Ni_7 by XRD on samples that was annealed at 1223 K for 600 h. Skakov et al. [80] studied the influence of cooling rate on formation of phases, which are not considered in the present study due to the non-equilibrium conditions. Savin [81] found C15, C36, and μ through quenching

Table 4
Predicted invariant reactions in the Fe-Nb system by the present CALPHAD modeling in comparison with available experiments [118,119].

Type	Compositions (at. % Nb)					Temp. (K)	Source
Congruent	Liquid	↔	C14				
	33.3		33.3			1903	This study
	33.5		33.5			1915	Pan et al. [20]
	33.3		33.3			1918	Expt. [11]
						1923-1933	Expt. [63]
						1903±5	Expt. [22,23]
Peritectic	Liquid	+	C14	↔	μ		
	52.7		38.0		49.1	1794	This study
	51.9		38.0		47.7	1814	Pan et al. [20]
	52.0		37.6		46.5	1796±2	Expt. [21]
	56.0		37.0		49.0	1793	Expt. [23]
Eutectic	Liquid	↔	μ	+	BCC_A2		
	58.3		51.6		91.0	1774	This study
	60.0		50.5		89.2	1773	Pan et al. [20]
	58.6		51.0		91.0	1781	Expt. [21]
	59.0		54.0		93.0	1773	Expt. [23]
Eutectic	Liquid	↔	BCC_A2	+	C14		
	9.1		3.0		26.9	1650	This study
	8.9		2.6		26.5	1654	Pan et al. [20]
	8.2±0.7		3.2		25.1	1646±1	Expt. [21]
	10.6		3.3		32.0	1643	Expt. [23]
	11.3-11.7		7.6		33.9	1629	Expt. [63]
	9.8					1638	Expt. [62]
	12.0		3.3			1643±1	Expt. [66]
	10.6					1645±2	Expt. [65]
	10					1621	Expt. [61]
Eutectic	BCC_A2	↔	FCC_A1	+	C14		
	2.0		1.5		27.3	1476	This study
	1.5		0.9		26.9	1466	Pan et al. [20]
	1.5		1.1				
		26.5	1456±15	Expt. [21]			
	1.3		0.1		33.9	1493	Expt. [63]
	6.3		1.0		32.0	1463	Expt. [23]
	10.		1.6			1481	Expt. [66]
						1473	Expt. [65]
						1463	Expt. [68]
						1493	Expt. [64]
Eutectic	FCC_A1	+	C14	↔	BCC_A2		
	0.7		28.0		1.0	1230	This study
	0.3		27.9		0.6	1222	Pan et al. [20]
			27.6			1216±25	Expt. [21]
	0.5		34.8		3.1	1238	Expt. [63]
	0.4		32.0		0.7	1223	Expt. [23]
						1262	Expt. [64]
						1223	Expt. [68]

directly from the melting temperature by XRD and SEM with EDX. However, the quenching rate was very high (100-1000 K/s), resulting in the formation of non-equilibrium phases like C15 and C36. Ueyama et al. [82] annealed the 10.0Fe-15.0Nb-75.0Ni alloy at 1473 K for 240 h and observed the formation of δ and FCC_A1 by XRD and EPMA. Takeyama et al. [83] annealed seven different alloys and four compositions later [43] at 1473 K for 240 h and reported the formation of FCC_A1, δ, C14, and μ via XRD and EPMA. Hasebe et al. [44] annealed eight different alloys at 1473 K for 240 h and 1373 K for 480 h and reported a ternary compound with the A_3B-stoichiometry, ordered hexagonal hP24 phase based on XRD, SEM, EPMA, and WDS in the composition range of (18.7-21.7)Fe-21.5Nb-(56.8-59.8)Ni. This phase is also observed experimentally in the present study and is considered as a stable phase in the present CALPHAD modeling. The experimental data from Takeyama et al. [43,83], Hasebe et al. [44] and Ueyama et al. [82] are used in the present assessment since the samples were annealed at high temperatures for at least 240 h.

4. Methodology

4.1. Experimental procedure

In diffusion multiples, several pure elements or alloy blocks are assembled to form solid solutions and intermetallic compounds at high temperatures [84–89]. This approach can incorporate many binary, ternary and multicomponent systems in one sample. In the present study, the isothermal section of the Fe-Nb-Ni system at 1373 K was investigated using this approach with the diffusion multiple shown Fig. 6.

The surfaces of the blocks were well polished before assembled and a hot isostatic pressing (HIP) run was performed to ensure the close interfacial contact between and among the metal blocks. The sample was then encapsulated in a quartz tube and annealed at 1373 K for 1000 hours, followed by water quenching to ambient temperature. A slice of the annealed sample was cut using electrical discharge machining (EDM), mounted, and polished with 0.05 μm silica suspension at the final step. Backscattered electron (BSE) images were taken using the XEIA3 TESCAN SEM with a voltage of 10 kV. The compositions in the Fe-Nb-Ni area were measured by EPMA line scan and WDS X-ray mapping

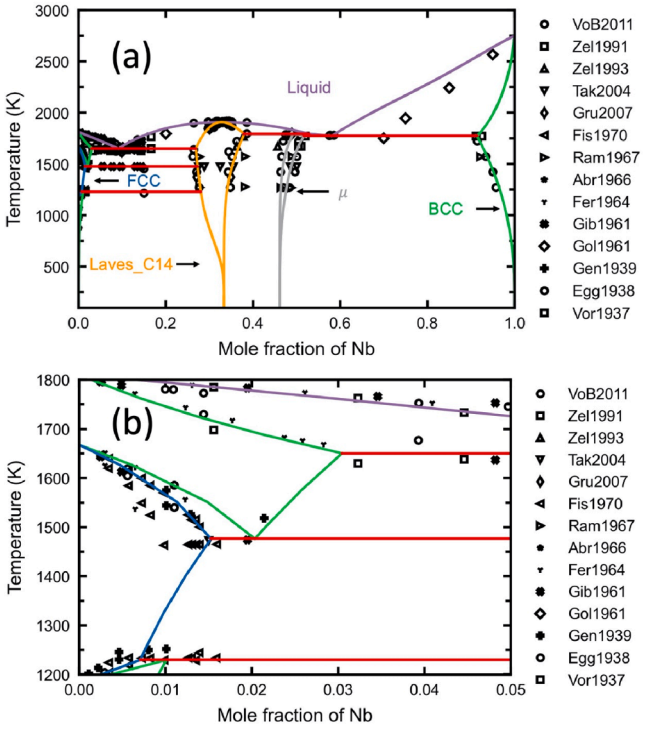

Fig. 5. (a) Calculated phase diagram of Fe-Nb from the present CALPHAD modeling superimposed with the experiments data [21–23,43,62–71]. (b) Calculated phase diagram of Fe-Nb (0.0 at. % Nb – 5.0 at. % Nb, 1200 K – 1800 K) from the present CALPHAD modeling superimposed with the experiments data [21–23,43,62–71].

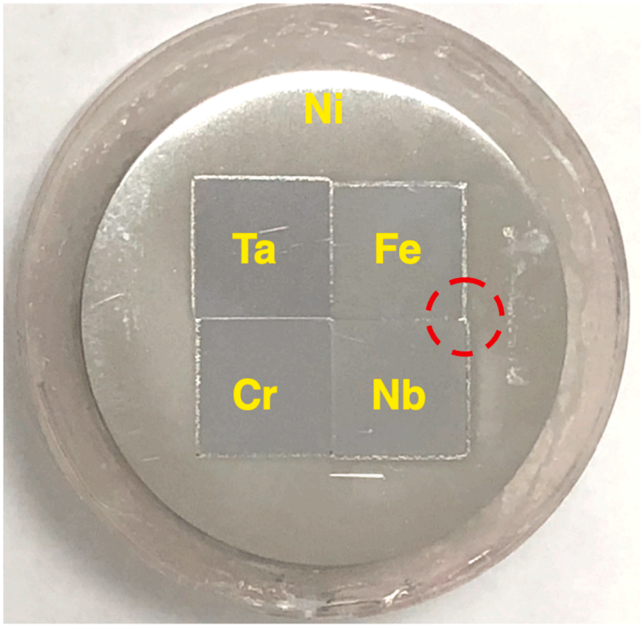

Fig. 6. Photograph of a slice cut from the diffusion multiple after heat treatment at 1373 K for 1000 hours. The Fe-Nb-Ni ternary location is marked by the open red circle. (For interpretation of the references to colour in this figure legend, the reader is referred to the web version of this article.)

with an accelerated voltage of 20 kV and beam current of 50 nA on Cameca SX100 to obtain the tie-lines under the assumption of local equilibrium at the phase interfaces.

4.2. Frist-principles calculations

Helmholtz energy of a given atomic and spin configuration as a function of temperature and volume can be predicted using the DFT-based quasiharmonic approach as follows [90]:

$$F(V,T) = E_0(V) + F_{vib}(V,T) + F_{el}(V,T) \quad (1)$$

where F represents the Helmholtz energy, V the volume, T the absolute temperature, $E_0(V)$ the static energy at 0 K without vibrational contribution as a function of volume, F_{vib} the contribution from lattice vibrations as a function of V and T, and F_{el} the contribution from thermal electrons as a function of V and T. The equilibrium volume at each temperature can be determined by solving $-\frac{\partial F}{\partial V} = P$ for a given pressure P.

Each endmember in a phase with sublattices represents one configuration. The values of $E_0(V)$ for each configuration were obtained at seven volumes around its equilibrium volume and fitted by the 4-parameter Birch-Murnaghan (BM4) equation of state [46],

$$E_0(V) = k_1 + k_2 V^{-2/3} + k_3 V^{-4/3} + k_4 V^{-2} \quad (2)$$

in which k_1, k_2, k_3, and k_4 are fitting parameters. The bulk modulus and the pressure derivative of bulk modulus can be obtained from the equation.

The vibrational contribution F_{vib} was obtained by the phonon density of states (pDOS) [91],

$$F_{\mathrm{vib}}(T,V) = k_B T \int_0^{\infty} \ln\left[2\sinh\frac{\hbar\omega}{2k_B T}\right] g(\omega)\, d\omega \quad (3)$$

where $g(\omega)$ is the pDOS as a function of V and frequency ω. The thermal electronic contribution F_{el} was calculated using the Mermin statistics, where F_{el}=$E_{el} - TS_{el}$ with E_{el} and S_{el} being the internal energy of thermal electrons and the bare electronic entropy, respectively [91].

All DFT-based first-principles calculations in the present study were performed using the Vienna *ab initio* Simulation Package (VASP) [92]. The electron-ion interaction was simulated through the projector augmented wave (PAW) method [93], while the exchange-correlation functional was depicted using the generalized gradient approximation (GGA) by Perdew, Burke, and Ernzerhof (PBE) [94]. The 368 eV was adopted as the plane-wave cutoff energy for structural relaxations, and the 520 eV for the final static calculations to get accurate *E-V* data. 6×10^{-5} eV/atom was the convergence criterion of the electronic self-consistency for relaxations and static calculations. The k-point meshes ($8 \times 8 \times 7$), ($5 \times 5 \times 1$), and ($9 \times 9 \times 5$) were used for relaxations and static calculations of δ, μ, and C14 phases, respectively. The pure BCC Nb, FCC Ni, and BCC Fe were considered as reference states. The number of endmembers is 27, 243, and 27 for δ, μ, and C14 phases, respectively. Their crystal structures are taken from Materials Project [57]. The ferromagnetic spin-polarization are considered for both Fe and Ni atoms. Phonon calculations were performed for the endmembers of C14-$Fe_1Nb_2Fe_3$ and μ-$Nb_6Nb_6Nb_6Fe_{18}Fe_3$ as their enthalpies of formation are negative. The supercells for phonon calculations were ($2 \times 2 \times 2$) for C14 with respect to its crystallographic cell and ($2 \times 2 \times 1$) for μ, where the employed k-point meshes were ($2 \times 2 \times 2$) and ($1 \times 1 \times 1$), respectively.

4.3. Machine Learning

ML was also employed to provide thermochemical data [95–97] as a comparison with DFT values. In the present study, all configurations of μ phases were predicted by ML using the light model from SIPFENN [97] and the model from Alignn [96]. SIPFENN [97] is an open-source ML tool to predict enthalpy of formation with input as structural files including atomic species and crystallographic information. The light

model in SIPFENN [97] was trained using OQMD data [56,98] with the mean absolute error (MAE) of 41.9 meV/atom. Similarly, the enthalpy of formation from Alignn [96] also only needs structural files, but Alignn [96] was trained based on the properties from JARVIS (Joint Automated Repository for Various Integrated Simulations) [99] with the MAE of 26.06 meV/atom. However, the results from ML only match well with those from DFT in stable endmembers. There is large discrepancy between values from ML and those from DFT in nonstable endmembers. Therefore, ML values is not used in the present study. Detailed comparisons between all configurations of μ phase in Fe-Nb-Ni from DFT, SIPFENN [97], and Alignn [96] are given in the Supplemental Material Fig. S2.

4.4. CALPHAD modeling

Eight phases were considered in the present study, i.e., liquid, BCC_A2, FCC_A1, FCC_L1$_2$, FCC_L1$_0$, hP24, C14, δ, and μ. The Gibbs energy functions of the pure elements (i.e., Fe, Nb, and Ni) were taken from the SGTE database [36]. There were four types of phases, i.e., disordered solution phases, ordered solution phases, stoichiometric phases, and non-stoichiometric phases, which were all modeled with the compound energy formalism [100].

The Gibbs energy of disordered solution phases, i.e., liquid, BCC_A2, and FCC_A1 can be represented by the Redlich-Kister polynomial [101] as follows,

$$\begin{aligned} G_m^{\alpha} = {} & x_{Fe}G_{Fe}^{\alpha} + x_{Nb}G_{Nb}^{\alpha} + x_{Ni}G_{Ni}^{\alpha} + RT(x_{Fe}lnx_{Fe} + x_{Nb}lnx_{Nb} + x_{Ni}lnx_{Ni}) \\ & + x_{Fe}x_{Nb}\sum_{k=0}^{k} L_{Fe,Nb}(x_{Fe} - x_{Nb})^k + x_{Fe}x_{Ni}\sum_{k=0}^{k} L_{Fe,Ni}(x_{Fe} - x_{Ni})^k \\ & + x_{Nb}x_{Ni}\sum_{k=0}^{k} L_{Nb,Ni}(x_{Nb} - x_{Ni})^k \\ & + x_{Fe}x_{Nb}x_{Ni}\left(x_{Fe}{}^{Fe}L_{Fe,Nb,Ni} + x_{Nb}{}^{Nb}L_{Fe,Nb,Ni} + x_{Ni}{}^{Ni}L_{Fe,Nb,Ni}\right) \end{aligned} \quad (4)$$

where x_{Fe}, x_{Nb} and x_{Ni} are the mole fractions of Fe, Nb, and Ni in phase α; G_{Fe}^{α}, G_{Nb}^{α}, and G_{Ni}^{α} are the molar Gibbs energies of Fe, Ni, and Nb with respect to their stable-element reference (SER) states at $P = 1$ bar and $T = 298.15$ K; R is the gas constant; ${}^kL_{i,j}$ denotes the kth binary interaction parameter between element i and j; and ${}^iL_{Fe,Nb,Ni}$ is the ternary interaction parameter for element i. All interaction parameters are modeled by $a + bT$.

As in the Fe-Ni binary system [35], FCC_A1, FCC_L1$_2$, and FCC_L1$_0$ are modelled using one Gibbs energy model with contributions from the disordered FCC_A1 phase $G_m^{A1}(x_s)$ described by the Redlich-Kister polynomial [101], and the ordering contribution described by the split compound energy formalism [102]. This can be expressed as follows:

$$G_m^{fcc} = G_m^{A1}(x_s) + G_m^{order}\left(y_s^1, y_s^2, y_s^3, y_s^4\right) - G_m^{order}\left(y_s^n = x_s\right) \quad (4a)$$

$G_m^{order}(y_s^1, y_s^2, y_s^3, y_s^4)$ represents the Gibbs energy described by the four-sublattice compound energy model, and $G_m^{order}(y_s^n = x_s)$ is the disordered component of $G_m^{order}(y_s^1, y_s^2, y_s^3, y_s^4)$. x_s represents the mole fraction of an element S and y_s^n the site fraction of element S on the n-th sublattice. The ordered contribution is obtained by reducing the disordered contribution $G_m^{order}(y_s^n = x_s)$ from the Gibbs energy of the four-sublattice model ($G_m^{order}(y_s^1, y_s^2, y_s^3, y_s^4)$). In this study, the ordering contributions of FCC_L1$_2$ and FCC_L1$_0$ in the Fe-Ni system are implemented based on the study of Ohnuma et al. [35]. This model has been implemented into the open-source PyCalphad [103,104].

The hP24 phase is modeled as a stoichiometric compound with its Gibbs energy per mole of formula described by,

$$G_{Fe:Nb:Ni}^{hP24} = 0.226 * {}^0G_{Fe}^{BCC} + 0.216 * {}^0G_{Nb}^{BCC} + 0.558 * {}^0G_{Ni}^{FCC} + A + BT \quad (5)$$

where A and B are model parameters, and ${}^0G_{Fe}^{BCC}$, ${}^0G_{Nb}^{BCC}$ and ${}^0G_{Ni}^{FCC}$ are Gibbs energies of BCC Fe, BCC Nb and FCC Ni.

The C14, δ, and μ phases exhibit composition homogeneity ranges, and their sublattice models are based on their Wyckoff sites as shown in Table 1. Their Gibbs energies per mole of formula unit are modeled as follows

$$G_{mf} = {}^0G_{mf} + RT\sum_t a^t \sum_i y_i^t lny_i^t + {}^EG_{mf} \quad (6)$$

In this equation, ${}^0G_{mf}$ is the Gibbs energy contribution from all endmembers based on the sublattice model calculated by summation of the product of site fraction (y_i^t) of each component (i) in its sublattice and the Gibbs energy of the corresponding endmember (${}^0G_{em}$), i.e., ${}^0G_{mf} = \sum_{em}\left(\prod_t y_i^{t0}\, G_{em}\right)$. The second term corresponds to the sum of ideal mixing from each sublattice, i.e., $\sum_i y_i^t lny_i^t$, weighted by the number of the sublattice sites, i.e., a^t. ${}^EG_{mf}$ represents the excess Gibbs energy including two types of contributions: first, mixing of two or more components in one sublattice with only one component in each of the other sublattices; second, mixing of two or more components simultaneously in more than one sublattices. In the present study, only the first type is considered as the second part is usually used to describe short-range ordering [105]. The first type of interaction is expressed as follows:

$${}^EG_{mf} = \sum_t \prod_{s\neq t} y_l^s \sum_{i>j}\sum_j y_i^t y_j^t L_{i,j:l}^t \quad (7)$$

where $L_{i,j:l}^t$ denotes the interaction parameter between components i and j in sublattice t while the other sublattices (s) contain only one component in each sublattice.

5. Results and discussion

5.1. Thermodynamic properties of Fe-Nb

Fig. 1 plots the enthalpy of formation ($\Delta_f H$) in Fe-Nb from the present CALPHAD modeling and the CALPHAD modeling by Pan et al. [20] in comparison with various DFT-based calculations from OQMD [56], the Materials Project [57], Liu et al. [16], Mathon et al. [11], and the present study; as well as experimental data from Meschel et al. [45] at 1373 K, Syutkin et al. [48], Drobyshev et al. [46] at 1224 – 1393 K, and Barbi et al. [47] at 1000 – 1400 K. As mentioned in Section 3.1, the data from Syutkin et al. [48] and DFT values were used in the present modeling. The results from DFT-based calculations at 0 K (-14.5 to -12.1 kJ/mole-atom at 33.3 at. % Nb and -13.5 to -9.5 kJ/mole-atom at 46.2 at. % Nb) show less than 1 kJ/mole-atom discrepancy from the experiments by Syutkin et al. [48] (-13.6 kJ/mole-atom at 33.3 at. % Nb). Nonetheless, the CALPHAD modeling employed in this study demonstrates a favorable agreement with experimental data by Syutkin et al. [48], exhibiting an average difference of 0.5 kJ/mole-atom, with measurements by Syutkin et al. [48]. Meanwhile, $\Delta_f H$ from Pan et al. [20] shows 1.63 kJ/mole-atom difference with measurements by Syutkin et al. [48].

Fig. 3 (a) plots the enthalpy of mixing (ΔH_{mix}) values in liquid at 1935 K from the present and Pan et al.'s [20] CALPHAD modeling in comparison with experimental data by Iguchi et al. [58] at 1873 K and by Schaefers et al. [60] at 1935 K and 2035 K. Fig. 3 (b) plots the activity values of Fe at 1873 K from the present and Pan et al.'s [20] CALPHAD modeling in comparison with experimental data by Ichise and Horikawa [58]. Both CALPHAD modeling results are in good agreement with experimental ΔH_{mix} with the difference less than 2 kJ/mol-atom. Similarly, both modeling results from the present study and Pan et al. [20] agree reasonably well with experimental activity data by Ichise and Horikawa [58]. The present modeling results match better with experimental data at 67.0 – 76 at. % Nb, while the results from Pan et al. [20] have a better agreement with the experiments at 37.0 – 40 at. % Nb.

Fig. 4 shows the heat capacities of C14 at 33.3 at. % Nb and μ at 46.2 at. % Nb between 348 and 1038 K from both the present and Pan et al.'s

[20] CALPHAD modeling in comparison with experimental data from Silva et al. [24] and phonon results of C14-$Fe_1Nb_2Fe_3$ and μ-$Nb_6Nb_6Nb_6Fe_{18}Fe_3$ endmembers from the present study. The present modeling used the data by Silva et al. [24], resulting in differences from 348 to 1038 K being 0.11 J $K^{-1}mol^{-1}$ for C14 and 0.25 J $K^{-1}mol^{-1}$ for μ within the deviations of three measurements of 0.05 – 0.48 for C14 and 0.04 – 0.42 for μ. At the same time, phonon calculations demonstrate a favorable agreement within the temperature range of 348 – 698 K when compared to experimental data by Silva et al. [24]. The differences between calculation from this study and experimental data are 0.23 J $K^{-1}mol^{-1}$ for C14 and 0.55 J $K^{-1}mol^{-1}$ for μ. The differences between calculation from this study and experimental data are 0.27 J $K^{-1}mol^{-1}$ for C14 and 0.46 J $K^{-1}mol^{-1}$ for μ. However, discrepancy increases in the temperature range of 733 – 1038 K, where the phonon calculations deviate from the experimental data by Silva et al. [24]. The differences in this range are 1.19 J $K^{-1}mol^{-1}$ for C14 and 1.52 J $K^{-1}mol^{-1}$ for μ. It should be nored that the phonon calculations are for one endmember only, while the calcualtions from the CALPHAD "odel' have contributions from all endmebers and more configurations in addition to the ground-state configuration as postulated by the zentropy theory [106–108].

5.2. Phase equilibria of Fe-Nb

Table 4 summarizes the calculated invariant reactions from both the present modeling and that by Pan et al. [20] in comparison with available experimental data [21–23,62–67,69]. The present modeling agrees well with experimental data with the composition differences less than 1.7 at. % Nb and the variance of reaction temperatures less than 1 K [21–23,62–67,69]. In the modeling study by Pan et al. [20], the difference in compositions is up to 1.8 at. % Nb, with the variance of reaction temperatures up to 6 K [21–23,62–67,69] from different experiments [21–23,62–67,69].

Fig. 5 (a) shows the calculated phase diagram from the present CALPHAD modeling with the experimental data superimposed [21–23, 43,62–71]. Fig. 5 (b) presents the calculated phase diagram of Fe-Nb from 0.0 at. % Nb – 5.0 at. % Nb and 1200 K – 1800 K) from the present CALPHAD modeling. The present model parameters are summarized in the thermodynamic database (TDB) file in the Supplemental Material. It can be seen from Fig. 5 (a) that the present thermodynamic description can reproduce well experimental data in terms of phase compositions and temperatures of invariant reactions. The phase boundaries between C14 and μ from Raman et al. [70] show around 2 at. % Nb deviation from the data by Voβ et al. [21], Takeyama et al. [43],

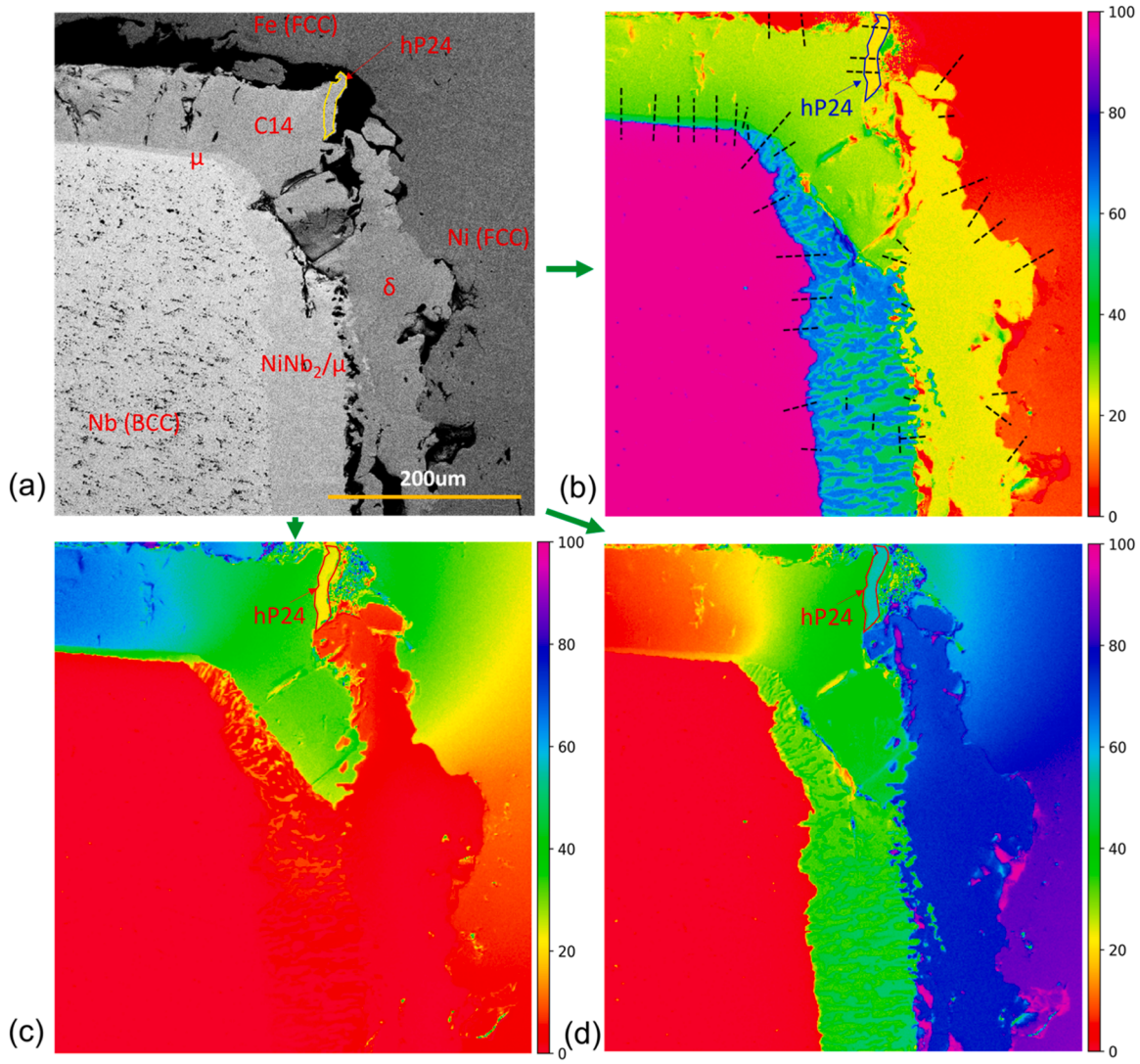

Fig. 7. (a) SEM BSE image of the Fe-Nb-Ni diffusion triple region of the diffusion multiple; The composition heatmaps of (b) Nb, (c) Fe, and (d) Ni in atomic percent using WDS. The black dash lines across phase interfaces in (b) are where the tie-lines were extracted based on the information of both the BSE image and the composition heatmaps.

Zelaya et al. [23], and Grunner et al. [71] are not reproduced. The liquidus data for BCC_A2 by Goldschmidt et al. [62] are high in Nb composition (70.0 at. % Nb at 1751 K) comparing with the eutectic reaction at 1773 - 1781 K of liquid, (58.6 – 59.0 at. % Nb) ↔ μ (51.0 – 54.0 at. % Nb) + BCC_A2 (91.0 – 93.0 at. % Nb), as shown in Table 4, and thus not reproduced by the present and Pan et al.'s [20] CALPHAD modeling. However, the present modeling shows a better match with the data by Goldschmidt et al. [62] with a difference around 185 K while it is 275 K by Pan et al. [20]; see Fig. 5 (a/b) and Fig. S3.

5.3. Experimental data for Fe-Nb-Ni at 1373 K

Fig. 7 (a) shows the SEM-BSE image of the triple-junction area in the Fe-Nb-Ni system after annealing at 1373 K for 1000 h. Fig. 7 (b), (c), and (d) plot the composition heatmaps of Nb, Fe, and Ni measured using the WDS mapping technique, respectively. Near the Fe-Nb binary region in the upper left of Fig. 7 (a), two layers of phases are observed and identified as C14 and μ, respectively, in terms of the WDS mapped compositions and the existing Fe-Nb phase diagram. In the Fe-Ni binary region, it is a single FCC phase. The phase analysis is complex for the Nb-Ni binary area due to the occurrence of the metastable Nb_2Ni phase. The formation of Nb_2Ni was also found by Zhao et al. [109]. However, our recent study [25] showed that the $\Delta_f H$ of Nb_2Ni is 15.47 kJ/atom higher than the convex hull in the Nb-Ni system. Therefore, the Nb_2Ni is considered as a metastable phase in the present study. Some data in the composition mapping are inaccurate due to the cracks as shown the BSE image in Fig. 7 (a). In the lower area of Fig. 7 (b), the blue and red areas alternatively appear in the Nb-Ni region, which were identified as the Nb_2Ni and μ phases, respectively. The δ-Ni_3Nb phase was also identified.

A ternary compound was found at the top-middle area. Its Nb content is close to that in δ-Ni_3Nb, as shown in Fig. 7 (b), but its Fe and Ni contents are distinctly different from those in δ-Ni_3Nb, and other phases according to Fig. 7 (c) and (d). The previous XRD analysis in the literature identified it as hP24 [110], which is adopted in the present study.

The tie-lines were extracted based on the composition-versus-distance profiles along the black dashed lines across the phase interfaces in Fig. 7 (b) and Fig. S4 (b). The isothermal section of Fe-Nb-Ni without the metastable Nb_2Ni phase at 1373 K is thus constructed and presented in Fig. 8. Two sets of tie-line data from the EPMA line scans and WDS mapping are consistent. The solubility of Fe in δ is around 8.5 at. % Nb, and the C14 extends deeply towards Ni, up to 44.5 at. % Ni. The Ni primarily replaces Fe in C14. The composition of the ternary compound, hP24, is about 22.9Fe-21.0Nb-56.1Ni in good agreement with the composition (18.7-21.7)Fe-21.5Nb-(56.8-59.8)Ni reported in the literature [110]. The μ phase has a significant solubility of Ni, up to 23.4 at. % Ni. Due to the formation of Nb_2Ni, the μ phase in Fe-Nb and Nb-Ni binary sides were separated. As presented in the isothermal section including the metastable Nb_2Ni in Fig. S5, the Nb_2Ni-(C14-Fe_2Nb) tie-lines prevents the extension of μ from the Nb-Ni binary side towards the Fe-Nb binary side, and thus the formation of metastable three-phase regions, i.e., Nb_2Ni-μ^{Ni7Nb6}-δ, Nb_2Ni-μ^{Fe7Nb6}-C14-Fe_2Nb, and Nb_2Ni-μ^{Fe7Nb6}-BCC_A2.

Our experimental data and the collected literature data of the Fe-Nb-Ni system at 1373 K are presented in Fig. 9. Overall, the experimental tie-line data agree well with the literature data. Our constructed isothermal section is comprehensive because of the large amount of tie-line data for all the phases in the system. The tie-lines related to C14 and μ phases are well mapped, providing critical information in improving the modeling of TCP phases.

5.4. First-principles calculations of Fe-Nb-Ni

Fig. 10 (a/b/c) show $\Delta_f H$ of 27, 27, and 243 endmembers of C14, δ and μ from the present DFT-based calculations at 0 K, respectively, and depict the lowest $\Delta_f H$ at 54.0Fe-46.0Nb-0.0Ni and 0.0Fe-54.0Nb-46.0Ni for μ, 0.0Fe-25.0Nb-75.0Ni for δ, and 0.0Fe-33.3Nb-66.7Ni and 66.7Fe-33.3Nb-0.0Ni for C14, respectively. Specific values of DFT calculations for C14, δ and μ can be found in the supplementary materials. Fig. 10 (d) plots the corresponding convex hull of $\Delta_f H$ at 0 K for all phases including C14, δ and μ, showing that δ is stable at around 0.0Fe-25.0Nb-75.0Ni, while μ is stable at around 54.0Fe-46.0Nb-0.0Ni and 0.0Fe-54.0Nb-46.0Ni, and C14 is stable at around 66.7Fe-33.3Nb-0.0Ni. From Fig. 10 (a/b/c/d), it can be see that the convex hull is formed by the most stable endmembers in each phases. The locations of stable phases show a good match with the convex hull predicted from the present DFT-based calculations, which agree with the experimental data.

5.5. Thermodynamic modeling of Fe-Nb-Ni

In the present study, the open-source software tools PyCalphad [103,

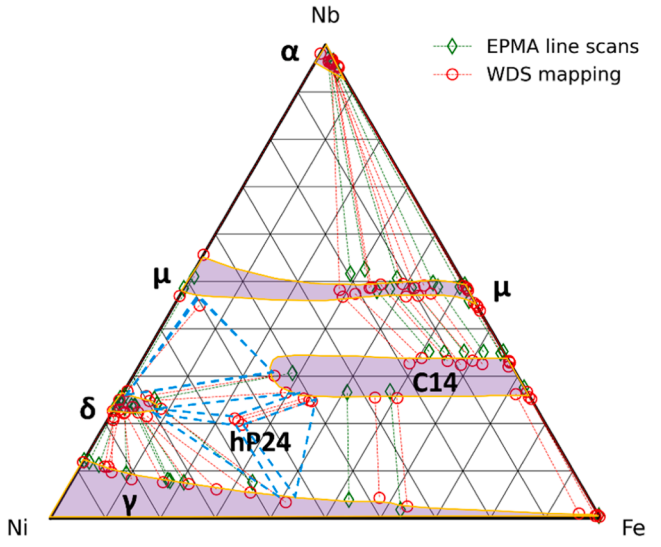

Fig. 8. Measured isothermal section of Fe-Nb-Ni at 1373 K. The green-colored tie-line data are from the EPMA line scans, and the red-colored tie-line data are from the WDS mapping. The purple-shadowed area with an orange boundary represents a single-phase region. The cyan-colored dashed triangles are the ternary phase regions. The ternary diagram is plotted in at.% with numbers removed for simplicity. (For interpretation of the references to colour in this figure legend, the reader is referred to the web version of this article.)

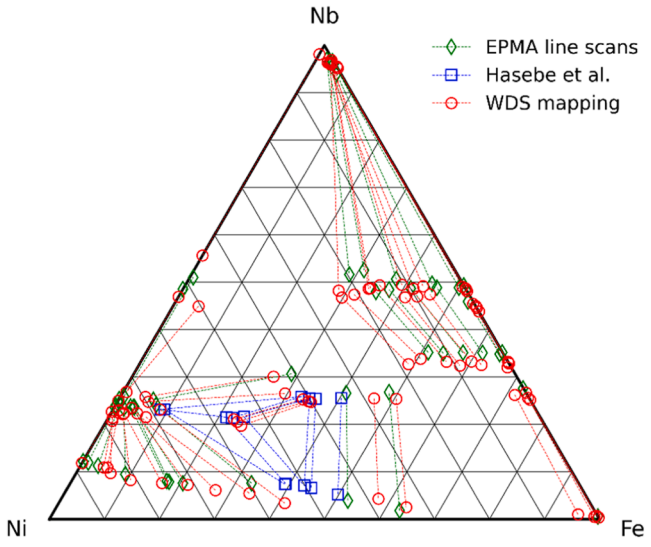

Fig. 9. Measured isothermal section of Fe-Nb-Ni at 1373 K in comparison with the literature data [110].

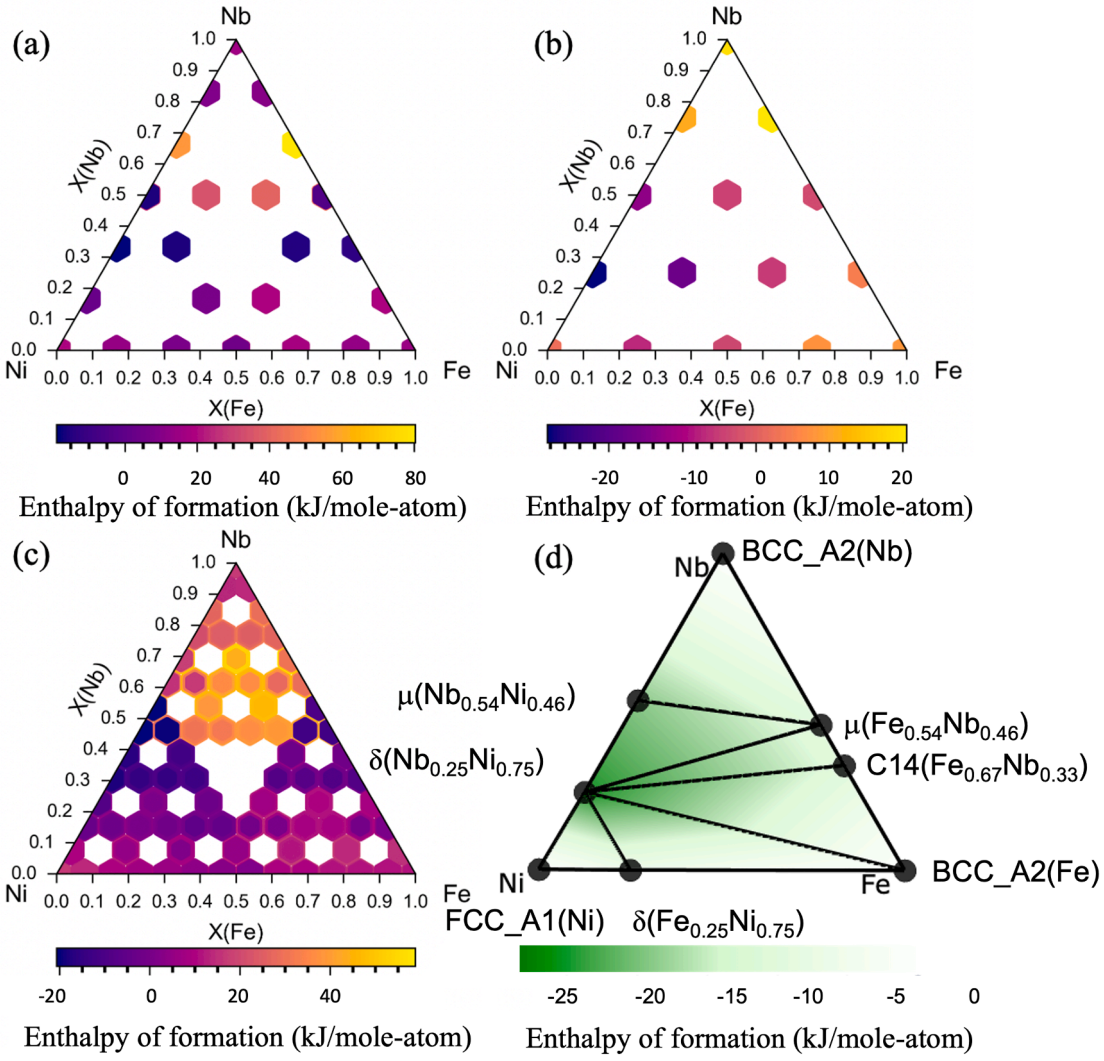

Fig. 10. Predicted ΔH_{form} of endmembers in Fe-Nb-Ni from DFT-based calculations, (a) 27 endmembers of C14 with the sublattice model $(Fe,Nb,Ni)_1(Fe,Nb,Ni)_2(Fe,Nb,Ni)_3$; (b) 27 endmembers of δ with the sublattice model $(Fe,Nb,Ni)_1(Fe,Nb,Ni)_1(Fe,Nb,Ni)_2$. (c) 243 endmembers of μ with the sublattice model $(Fe,Nb,Ni)_1(Fe,Nb,Ni)_2(Fe,Nb,Ni)_2(Fe,Nb,Ni)_2(Fe,Nb,Ni)_6$. (d) The corresponding convex hull of ΔH_{form} of all phases.

104] and ESPEI [111,112] were utilized for the CALPHAD modeling of the Fe-Nb-Ni system. PyCalphad is a Python-based package that enables thermodynamic calculations using various thermodynamic models including user-customized models. ESPEI is designed for evaluation of model parameters, utilizing PyCalphad as the computational engine to perform thermodynamic calculations. ESPEI operates in two steps. First step is to generate model parameters of individual phases using thermochemical data. Secondly, the model parameters are refined using both thermochemical data and phase equilibrium data through Bayesian parameter estimation by an ensemble Markov Chain Monte Carlo (MCMC) approach [113–115].

For the Fe-Nb binary system, the $\Delta_f H$ values for C14 and μ, ΔH_{mix} for the liquid phase, and the heat capacity for C14 and μ were first used to generate the model parameters for each phase. Subsequently, the model parameters were optimized through MCMC in ESPEI, using both phase equilibrium and phase boundary information. Once the modeling of the Fe-Nb system is complete, the Fe-Nb-Ni system is constructed by combining the Fe-Nb, Fe-Ni, and Nb-Ni binary systems. The thermochemical data for single phases are then employed to generate model parameters, encompassing the $\Delta_f H$ values for C14, δ, and μ. These model parameters are subsequently refined through MCMC in ESPEI, utilizing phase equilibrium data including tie-lines in Fe-Nb-Ni at both 1373 K and 1473 K.

Fig. 11 shows the calculated isothermal sections at 1373 K and 1473 K from the present CALPHAD modeling and that by Mathon et al. [11], together with experimental data from the present EPMA line scans and WDS mapping and the data by Hasebe et al. [44] and Takeyama et al. [43]. Both the present CALPHAD modeling and that by Mathon et al. [11] show a good agreement with experimental data about phase boundaries between μ and BCC_A2, and between μ and C14 at 1373 K, as seen in Fig. 11 (a, b) along with the phase boundaries between δ, BCC_A2, and FCC_A1 phases. However, according to the experiments in the present study and by Hasebe et al. [44], C14 is observed from 30.0Fe-33.3Nb-36.7Ni to 66.7Fe-33.3Nb-0.0Ni, while in the modeling study by Mathon et al. [11] C14 is stable in a much smaller composition range from 37.6Fe-33.5Nb-28.9Ni to 65.8Fe-34.2Nb. In the present study C14 is stable from 27.0Fe-31.2Nb-41.8Ni to 66.7Fe-33.3Nb-0.0Ni, which in good agreement with the experiments from Hasebe et al. [44]. Furthermore, the phase boundary of μ in BCC_A2 + μ two-phase equilibria calculated from the present model (52.0Fe-48.0Nb-0Ni to 28.6Fe-53.2Nb-18.2Ni) agree well with the experimentally determined values (50.5Fe-49.5Nb-0Ni to 28.6Fe-51.6Nb-19.8Ni). While in the modeling study by Mathon et al. [11], it is narrower from 51.2Fe-48.8Nb-0Ni to 28.6Fe-49.0Nb-22.4Ni. As discussed in Section 3.3, hP24 is considered as a stable phase at 22.6Fe-21.6Nb-55.8Ni in the present study which matches with the present experiments

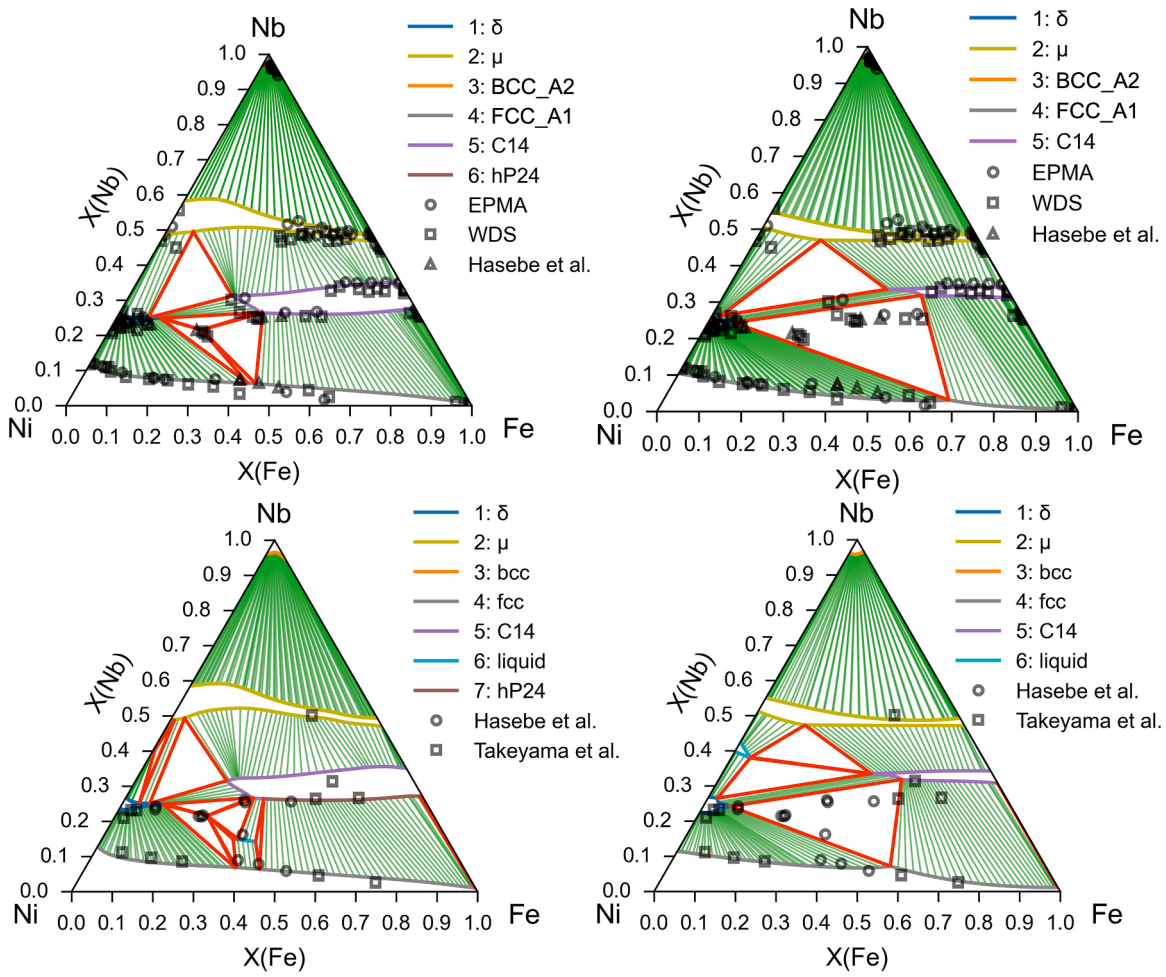

Fig. 11. (a) Calculated isothermal section of the Fe-Nb-Ni system at 1373 K superimposed with experimental data from this study and that of Hasebe et al. [44]; (b) Computed 1373 K isothermal section using the thermodynamic modeling of Mathon et al. [11] in comparison of the same experimental datasets; (c) Calculated 1473 K isothermal section from the present thermodynamic assessment superimposed with experimental data from Hasebe et al. [44] and Takeyama et al. [43]; and (d) Computed 1473 K isothermal section based on Mathon et al. [11] in comparison with experimental data from Hasebe et al. [44] and Takeyama et al. [43].

(22.9Fe-21.0Nb-56.1Ni) and those by Hasebe et al. [44] ((18.7-21.7) Fe-21.5Nb-(56.8-59.8)Ni.).

From the Fig. 11 (c, d), the phase boundaries between δ and FCC_A1 at 1473 K are reproduced by both the present and thermodynamic model from Mathon et al. [11]. However, Takeyama et al. [43] observed the liquid phase at 33.9Fe-16.3Nb-49.8Ni and predicted by the present study, which is not shown in the modeling results by Mathon et al. [11]. The broad composition range of C14 at 1473 K from 30.0Fe-33.3Nb-36.7Ni to 66.7Fe-33.3Nb-0.0Ni by Hasebe et al. [44] is well reproduced by the present modeling in the range of 23.2Fe-31.6Nb-55.2Ni to 66.7Fe-33.3Nb-0.0Ni, while it is much narrow from the model by Mathon et al. [11] in the range of 36.5Fe-33.5Nb-30.0Ni to 65.6Fe-34.4Nb-0.0Ni. Additionally, the present model depicts the presence of hP24 at 1473 K, which is in a good agreement with the data by Hasebe et al. [44].

5.6. Additional discussion

In the present study, sublattice models for C14, δ, and μ are built based on theirs Wyckoff positions. These comprehensive sublattice models have been proven to give an accurate description of the site fraction (the behavior of elements in each Wyckoff positions), as shown in the Nb-Ni binary system [25]. The ternary system is built upon on binaries, thus inaccuracies in binaries will be carried into the ternary. Therefore, even if no site fraction data are available for the Fe-Nb-Ni ternary system, the complete sublattice models are still critical to accurately describe the behavior of elements in each Wyckoff positions in C14, δ, and μ.

DFT calculations are used to provide $\Delta_f H$ for all endmembers in C14, δ, and μ. This approach not only provide more accurate value but also give a deeper atomistic understanding of the behavior of different elements in different phases. As mentioned in Section 3.1, $\Delta_f H$ of the Fe-Nb system from experiments have large differences. For examples, $\Delta_f H$ from EMF experiments are lower probably due to the NbO formation whereas values from direct reaction calorimetry are higher probably due to incomplete reactions. However, DFT offers more accurate values that agree with those from Syutkin et al. [48] using drop solution calorimetry. This agreement shows the accuracy of DFT. At the same time, $\Delta_f H$ from DFT are adopted instead of a random value of 5000 J/mol-atom for endmembers with one element in each sublattice [11]. Our choice of DFT values offers increased accuracy in thermodynamic properties and a more profound atomistic understanding of how different elements behave in various phases, enhancing the reliability and robustness of the overall modeling.

Fe-Nb-Ni is very useful for designing functionally graded materials (FGMs) transitioning from Ni-based superalloys to Fe-based superalloys, since C14, δ, and μ are the major TCP phases formed in both Ni-based superalloys and Fe-based superalloys. However, there is no reliable thermodynamic database in the intermediate composition region, as even commercial databases such as TCFE and TCNI are only valid at the

Fe or Ni rich corner [116]. With the complete sublattice model, DFT computations and new experimental data, the present study will not only predict the TCP phase formation, but also to provide many other parameters needed to simulate microstructure, processing and properties for FGMs including Fe and Ni based superalloys.

6. Conclusions

The present study shows a significant improvement in modeling both thermodynamic properties of the Fe-Nb and Fe-Nb-Ni systems using a combination of experimental and computational methods. A diffusion triple was employed to efficiently collect more data for the 1373 K isothermal sections of the Fe-Nb-Ni system, and DFT-based first-principles calculations to predict Gibbs energies of three TCP phases (Laves_C14, δ, and μ) in the Fe-Nb-Ni system. Through experimental measurements of phase boundaries of Fe-Nb-Ni, new sublattice models for the TCP phases, and the CALPHAD modeling for both the Fe-Nb and Fe-Nb-Ni systems, following main findings are obtained:

- The complete isothermal section of the Fe-Nb-Ni system at 1373 K was determined, filling the missing information of the TCP phases range;
- Enthalpy of formation for all endmembers of the C14, δ, and μ phases were calculated through first-principles calculations plus phonon properties of their stable endmembers, providing more accurate and precise values as well as a deeper atomistic insight for the TCP phases;
- Thermodynamic models of the C14, δ, and μ phases were built based on their Wyckoff positions for more accurate description of the TCP phases with three-, three- and five-sublattice models for C14, δ, and μ, respectively, resulting in an accurate description of the TCP phases; and
- Thermodynamic remodeling of the Fe-Nb and Fe-Nb-Ni systems was performed using DFT-based first-principles calculations, and experimental data from the present study and the literature. This study not only refines the thermodynamic modeling but also provides an understanding of thermochemical behavior in the Fe-Nb-Ni system, as well as reliable predictions of TCP phases.

Declaration of competing interest

The authors declare that they have no known competing financial interests or personal relationships that could have appeared to influence the work reported in this paper.

Acknowledgements

The authors thank John Donovan and Julie Chouinard for their help in performing WDS X-ray mapping and EPMA line scans at the CAMCOR Facilities of the University of Oregon and thank the AIMLAB in University of Maryland who provided the SEM technique support. The authors also thank Songge Yang from Worcester Polytechnic Institute for his help in analyzing phonon results. The experimental study at University of Maryland was funded by the National Science Foundation (NSF) Division of Civil, Mechanical and Manufacturing Innovation (CMMI) Award # CMMI-2004979. The authors at the Pennsylvania State University acknowledge the financial support by the Office of Naval Research (ONR) under Contract No. N00014-21-1-2608 and NSF via Award CMMI-2050069. First-principles calculations were performed partially on the Roar supercomputer at the Pennsylvania State University's Institute for Computational and Data Sciences (ICDS), partially on the resources of the National Energy Research Scientific Computing Center (NERSC) supported by the U.S. DOE Office of Science User Facility operated under Contract No. DE-AC02-05CH11231, and partially on the resources of the Extreme Science and Engineering Discovery Environment (XSEDE) supported by NSF with Grant No. ACI-1548562

Supplementary materials

Supplementary material associated with this article can be found, in the online version, at doi:10.1016/j.actamat.2024.119747.

References

[1] F.C. Frank, J.S. Kasper, Complex alloy structures regarded as sphere packings. I. Definitions and basic principles, Acta Crystallogr 11 (1958) 184–190, https://doi.org/10.1107/S0365110x58000487.
[2] J.H. Alano, R.L. Siqueira, A.D. de Oliveira, G. dos Santos Vacchi, C.A. Della Rovere, S.E. Kuri, Effect of TCP phase formation on the electrochemical corrosion behavior of the nickel-based superalloy UNS N26455, Corros. Sci. (2020) 177, https://doi.org/10.1016/j.corsci.2020.108965.
[3] P. Pandey, S.K. Makineni, A. Samanta, A. Sharma, S.M. Das, B. Nithin, C. Srivastava, A.K. Singh, D. Raabe, B. Gault, K. Chattopadhyay, Elemental site occupancy in the L12 A3B ordered intermetallic phase in Co-based superalloys and its influence on the microstructure, Acta Mater 163 (2019) 140–153, https://doi.org/10.1016/j.actamat.2018.09.049.
[4] E.P. George, W.A. Curtin, C.C. Tasan, High entropy alloys: A focused review of mechanical properties and deformation mechanisms, Acta Mater 188 (2020) 435–474, https://doi.org/10.1016/j.actamat.2019.12.015.
[5] N. Saini, R.S. Mulik, M.M. Mahapatra, Study on the effect of ageing on laves phase evolution and their effect on mechanical properties of P92 steel, Mater. Sci. Eng. A. 716 (2018) 179–188, https://doi.org/10.1016/j.msea.2018.01.035.
[6] H.M. Tawancy, Precipitation characteristics of μ-phase in wrought nickel-base alloys and its effect on their properties, J. Mater. Sci. 31 (1996) 3929–3936, https://doi.org/10.1007/BF00352653.
[7] S. Qin, T.C. Novak, M.K. Vailhe, Z.K. Liu, A.M. Beese, Plasticity and fracture behavior of Inconel 625 manufactured by laser powder bed fusion: Comparison between as-built and stress relieved conditions, Mater. Sci. Eng. A. 806 (2021) 140808, https://doi.org/10.1016/j.msea.2021.140808.
[8] T. Fang, S.J. Kennedy, L. Quan, T.J. Hicks, The structure and paramagnetism of Ni3Nb, J. Phys. Condens. Matter. 4 (1992) 2405–2414, https://doi.org/10.1088/0953-8984/4/10/007.
[9] P.I. Kripyakevich, E.I. Gladyshevskii, E.N. Pylaeva, Compounds of the W6Fe7 type in the Ta-Ni and Nb-Ni systems, Sov. Phys. Crystallogr. 7 (1962) 165–168.
[10] Z.K. Liu, First-principles calculations and CALPHAD modeling of thermodynamics, J. Phase Equilibria Diffus. 30 (2009) 517–534, https://doi.org/10.1007/s11669-009-9570-6.
[11] M. Mathon, D. Connétable, B. Sundman, J. Lacaze, Calphad-type assessment of the Fe–Nb–Ni ternary system, Calphad 33 (2009) 136–161.
[12] W. Huang, A Thermodynamic Evaluation of the Fe-Nb-C System/Eine Thermodynamische Auswertung des Systems Fe-Nb-C, Int. J. Mater. Res. 81 (1990) 397–404.
[13] B.J. Lee, Thermodynamic assessment of the Fe-Nb-Ti-CN system, Metall. Mater. Trans 32 (2001) 2423.
[14] G.C. Coelho, S.G. Fries, H.L. Lukas, P. Majewski, J.M.Z. Bejarano, S. Gama, C.A. Ribeiro, G. Effenberg, Thermodynamic optimization of the Nb-Fe and Ta-Fe binary systems, in: Klaus Schulze Symp. Process. Appl. High Purity Refract. Met. Alloy., 1994.
[15] S. Srikanth, A. Petric, A thermodynamic evaluation of the Fe-Nb system, Zeitschrift Für Met 85 (1994) 164–170.
[16] S. Liu, B. Hallstedt, D. Music, Y. Du, Ab initio calculations and thermodynamic modeling for the Fe-Mn-Nb system, Calphad Comput. Coupling Phase Diagrams Thermochem. 38 (2012) 43–58, https://doi.org/10.1016/j.calphad.2012.03.004.
[17] A.V. Khvan, B. Hallstedt, Thermodynamic description of the Fe-Mn-Nb-C system, Calphad Comput. Coupling Phase Diagrams Thermochem. 39 (2012) 62–69, https://doi.org/10.1016/j.calphad.2012.09.001.
[18] C. He, Y. Qin, F. Stein, Thermodynamic Assessment of the Fe-Al-Nb System with Updated Fe-Nb Description, J. Phase Equilibria Diffus. 38 (2017) 771–787, https://doi.org/10.1007/s11669-017-0566-3.
[19] C. Toffolon, C. Servant, Thermodynamic assessment of the Fe-Nb system, Calphad Comput. Coupling Phase Diagrams Thermochem. 24 (2000) 97–112, https://doi.org/10.1016/S0364-5916(00)00017-1.
[20] Q. Pan, W. Liu, T. Wu, W. Zheng, J. Wang, X.G. Lu, Thermodynamic reassessment of Fe–Nb–V system, Calphad Comput. Coupling Phase Diagrams Thermochem. 80 (2023) 102529, https://doi.org/10.1016/j.calphad.2023.102529.
[21] S. Vob, M. Palm, F. Stein, D. Raabe, Phase equilibria in the Fe-Nb system, J. Phase Equilibria Diffus. 32 (2011) 97–104, https://doi.org/10.1007/s11669-010-9808-3.
[22] J.M.Z. Bejarano, S. Gama, C.A. Ribeiro, G. Effenberg, C. Santos, On the Existence of the Fe2Nb3 Phase in the Fe-Nb System/Zur Existenz der Phase Fe2Nb3 im System Fe-Nb, Int. J. Mater. Res. 82 (1991) 615–620.
[23] J.M.Z. Bejarano, S. Gama, C.A. Ribeiro, G. Effenberg, The iron-niobium phase diagram, Int. J. Mater. Res. 84 (1993) 160–164.
[24] A.A.A.P. Silva, M.S. Lamoglia, G. Silva, J.M. Fiorani, N. David, M. Vilasi, G. C. Coelho, C.A. Nunes, L.T.F. Eleno, Heat capacity measurements of the Fe2Nb and Fe7Nb6 intermetallic compounds, J. Alloys Compd. 878 (2021) 160411, https://doi.org/10.1016/j.jallcom.2021.160411.
[25] H. Sun, S.L. Shang, R. Gong, B.J. Bocklund, A.M. Beese, Z.K. Liu, Thermodynamic modeling with uncertainty quantification in the Nb-Ni system using the upgraded PyCalphad and ESPEI, (2022). https://doi.org/10.48550/ARXIV.2204.11813.

[26] F. Hegg, Thermomagnetic Study of Ferro-nickels, Arch. Sci Phys. Nat. Geneve. 30 (1910) 15–45.
[27] J.S. March, The Alloys of Iron and Nickel, Vol. 1, (1938).
[28] O. Kubaschewski, Iron—Binary Phase Diagrams, Springer Science & Business Media, 2013.
[29] R. Jackson, The UN Founding Fathers and Dr Chisholm, Concepts Pract, Humanit. Med. 12 (2008) 137–140, https://doi.org/10.1007/978-0-387-72264-1_19.
[30] C.W. Yang, D.B. Williams, J.I. Goldstein, A revision of the Fe-Ni phase diagram at low temperatures (<400°C), J. Phase Equilibria. 17 (1996) 522–531, https://doi.org/10.1007/BF02665999.
[31] V. Kuznetsov, M.S.I.T. Report, Msi, Stuttgart. (2003).
[32] G. Cacciamani, J. De Keyzer, R. Ferro, U.E. Klotz, J. Lacaze, P. Wollants, Critical evaluation of the Fe-Ni, Fe-Ti and Fe-Ni-Ti alloy systems, Intermetallics 14 (2006) 1312–1325, https://doi.org/10.1016/j.intermet.2005.11.028.
[33] F. OSMOND, Experiments on Alloys of Iron and Nickel, in: Minutes Proc. Inst. Civ. Eng., Thomas Telford-ICE Virtual Library, 1899, pp. 312–327.
[34] M. Mitteilungen, U. Gbttingen, G. Tammann, H. Ed, Uber die Legierungen des Nickels und Kobalts mit Eisen., (n.d.).
[35] I. Ohnuma, S. Shimenouchi, T. Omori, K. Ishida, R. Kainuma, Experimental determination and thermodynamic evaluation of low-temperature phase equilibria in the Fe–Ni binary system, Calphad Comput. Coupling Phase Diagrams Thermochem. 67 (2019) 101677, https://doi.org/10.1016/j.calphad.2019.101677.
[36] A.T. Dinsdale, SGTE data for pure elements, Calphad 15 (1991) 317–425, https://doi.org/10.1016/0364-5916(91)90030-N.
[37] L. Kaufman, H. Nesor, Coupled phase diagrams and thermochemical data for transition metal binary systems — II, Calphad 2 (1978) 81–108, https://doi.org/10.1016/0364-5916(78)90006-8.
[38] A. Bolcavage, A Reassessment of the Calculated Ni-Nb Phase Diagram, J. Phase Equilibria. 17 (1996) 92–100.
[39] R. July, A thermodynamic calculation of the Ni-Nb phase diagram, 179 (1992) 177–185.
[40] H. Chen, Y. Du, Refinement of the thermodynamic modeling of the Nb–Ni system, Calphad 30 (2006) 308–315.
[41] J.M. Joubert, B. Sundman, N. Dupin, Assessment of the niobium–nickel system, Calphad 28 (2004) 299–306.
[42] C. Zhou, C. Guo, J. Li, C. Li, Z. Du, Key Experiments and Thermodynamic Description of the Co-Nb-Ni System, Metall. Mater. Trans. A Phys. Metall. Mater. Sci. 51 (2020) 5892–5911, https://doi.org/10.1007/s11661-020-05963-2.
[43] M. Takeyama, N. Gomi, S. Morita, T. Matsuo, Phase Equilibria and Lattice Parameters of Fe 2 Nb Laves Phase in Fe-Ni-Nb Ternary System at Elevated Temperatures, MRS Proc 842 (2004), https://doi.org/10.1557/PROC-842-S5.37. S5.37.
[44] Y. Hasebe, K. Hashimoto, M. Takeyama, Phase equilibria among γ-Fe/Fe2Nb (TCP)/Ni3Nb (GCP) phases in Fe-Ni-Nb ternary system at elevated temperatures, Nippon Kinzoku Gakkaishi/Journal Japan Inst. Met 75 (2011) 265–273, https://doi.org/10.2320/jinstmet.75.265.
[45] S.V. Meschel, O.J. Kleppa, The standard enthalpies of formation of some intermetallic compounds of transition metals by high temperature direct synthesis calorimetry, J. Alloys Compd. 415 (2006) 143–149, https://doi.org/10.1016/j.jallcom.2005.08.006.
[46] V.N. Drobyshev, T.N. Rezukhina, X-RAY INVESTIGATION OF THE NB-FE SYSTEM AND THE DETERMINATION OF THE THERMODYNAMIC PROPERTIES OF THE COMPOUND NBFE 2, Russ. Met (1966) 85–89.
[47] G.B. Barbi, High Temperature Electrochemical Determination of the Thermodynamic Stability of the Iron-Rich, Iron-Niobium Intermetallic Phase, Zeitschrift Fur Naturforsch. - Sect. A, J. Phys. Sci. 24 (1969) 1580–1585, https://doi.org/10.1515/zna-1969-1020.
[48] E.A. Syutkin, A. Jacob, C. Schmetterer, A.V. Khvan, B. Hallstedt, A.T. Dinsdale, Experimental determination of the thermodynamic properties of the Laves phases in the Cr-Fe-Nb system, Thermochim. Acta. 624 (2016) 47–54, https://doi.org/10.1016/j.tca.2015.12.001.
[49] P.R. Subramanian, J.F. Smith, Thermodynamics of formation of Y-Fe alloys, Calphad 8 (1984) 295–305.
[50] T.N. REZUKHINA, L.I. KRAVCHENKO, THERMODYNAMIC PROPERTIES OF THE LAVES PHASE TAFE 2, IZVEST AKAD Nauk SSSR Met. JAN.-FEB. 1971,–1–, 164–169. (1971).
[51] G.B. Barbi, Determination of thermodynamic stability of the Fe2Ta intermetallic phase by non-stationary emf measurements on solid galvanic chains, J. Less Common Met. 22 (1970) 487–494.
[52] V.N. Drobyshev, T.N. Rezukhina, THERMODYNAMIC PROPERTIES OF COBALT-COLUMBIUM ALLOYS, ZH FIZ KHIM. 39 (1965) 151–156.
[53] T.N. Rezukhina, L.I. Kravchenko, The thermodynamic properties of Laves phases in mixtures of Ta+ Co. Solid-electrolyte galvanic cell studies, J. Chem. Thermodyn. 4 (1972) 655–667.
[54] N.P. Lyakishev, Y.U.P. Snitko, V.I. Alekseev, G. Levshin, Free-Energy of Formation of the Intermetallic Ni sub 3 Nb, Russ, J. Phys. Chem. 57 (1983) 101–102.
[55] V.I. Alekseev, G.B. Petrov, G.V. Shcherbedinskij, Investigation into thermodynamic properties of Ni-Nb alloys, Izv. Akad. Nauk SSSR, Met. (1978) 59–62.
[56] S. Kirklin, J.E. Saal, B. Meredig, A. Thompson, J.W. Doak, M. Aykol, S. Rühl, C. Wolverton, The Open Quantum Materials Database (OQMD): assessing the accuracy of DFT formation energies, Npj Comput. Mater. 1 (2015) 1–15.
[57] A. Jain, S.P. Ong, G. Hautier, W. Chen, W.D. Richards, S. Dacek, S. Cholia, D. Gunter, D. Skinner, G. Ceder, Commentary: The Materials Project: A materials genome approach to accelerating materials innovation, APL Mater 1 (2013) 11002.
[58] Y. Iguchi, S. Nobori, K. Saito, T. Fuwa, CALORIMETRIC STUDY OF HEATS OF MIXING OF LIQUIDS IRON ALLOYS Fe-Cr, Fe-Mo, Fe-W, Fe-V, Fe-Nb, Fe-Ta, Tetsu-To-Hagane/Journal Iron Steel Inst. Japan. 68 (1982) 633–640, https://doi.org/10.2355/tetsutohagane1955.68.6_633.
[59] V.S. Sudavtsova, V.P. Kurach, G.I. Batalin, Thermochemical Properties of Molten Binary Fe–(Y, Zr, Nb, Mo) Alloys, Russ. Met (1987) 59–60.
[60] K. Schaefers, M. Roesner-Kuhn, J. Qin, M.G. Frohberg, Mixing enthalpy and heat content measurements of liquid binary iron-niobium alloys, Steel Res 66 (1995) 183–187, https://doi.org/10.1002/srin.199501109.
[61] E. Paul, L.J. Swartzendruber, The Fe-Nb (Iron-Niobium) system, Bull. Alloy Phase Diagrams. 7 (1986) 248–254, https://doi.org/10.1007/BF02869000.
[62] H.J. Goldschmidt, The constitution of the iron-niobium-silicon system, J. Iron Steel Inst. 194 (1960) 169–180.
[63] N.M. Voronov, Alloys of iron with niobium, Izv. Akad. Nauk SSSR, Otd. Mat. Estestv. Nauk. (1937) 1369–1379.
[64] H. Eggers, W. Peter, The iron-niobium phase diagram, Mitt. Kaiser-Wilhelm Inst. Eisenforsch. 20 (1938) 199–203.
[65] R. Genders, R. Harrison, Niobium-iron alloys, J. Iron Steel Inst. 140 (1939) 29–37.
[66] W.S. Gibson, J.R. Lee, W. Hume-Rothery, Liquidus-solidus relations in iron-rich iron-niobium and iron-molybdenum alloys, J. Iron Steel Inst.(London) 198 (1961).
[67] A. Ferrier, E. Ubelacker, E. Wachtel, Study of the Fe-Nb Phase Diagram Between 0 and 12 at% Nb from 1200 to 1535 C, CR Acad. Sci. Paris. 258 (1964) 5424–5427.
[68] E.P. Abrahamson, S.L. Lopata, THE LATTICE PARAMETERS AND SOLUBILITY LIMITS OF ALPHA IRON AS AFFECTED BY SOME BINARY TRANSITION-ELEMENT ADDITIONS, ARMY MATERIALS RESEARCH AGENCY WATERTOWN MASS (1966).
[69] Z. Kobalt, V.W.A. Fischer, K. Lorenz, H. Fabritius, Untersuchung der 19 (1970).
[70] A. Raman, Structural study of niobium-iron alloys, Proc. Indian Acad. Sci. - Sect. A. 65 (1967) 256–264, https://doi.org/10.1007/BF03049403.
[71] D. Grüner, Untersuchungen zur Natur der Laves-Phasen in Systemen der Übergangsmetalle, (2007).
[72] K.A. Peard, D.W. Borland, Precipitation in an Fe-40%Ni-6%Nb alloy, Scr. Metall. 3 (1969) 267–269, https://doi.org/10.1016/0036-9748(69)90317-2.
[73] K. Leitch, M. Chaturvedi, Aging behavior of Fe-30 Ni alloys containing niobium, Metall. Trans. 2 (1971) 1407–1413, https://doi.org/10.1007/BF02913368.
[74] J. Manenc, J. Bourgeot, H. de Boer, Structure et durcissement d'un alliage austenitique Fe - 30 % Ni - 5 % Nb, Scr. Metall. 2 (1968) 453–457, https://doi.org/10.1016/0036-9748(68)90193-2.
[75] I. Kirman, Comments on "structure et durcissement d'un alliage austenitique Fe-30% Ni-5% Nb, Scr. Metall 2 (1968) 679–680, https://doi.org/10.1016/0036-9748(68)90242-1.
[76] J. Manenc, Response a l'article de Kirman "structure et durcissement d'un alliage austenitique Fe-30% Ni-5% Nb, Scr. Metall. 2 (1968) 705, https://doi.org/10.1016/0036-9748(68)90250-0.
[77] W.E. Quist, C.J. van der Wekken, R. Taggart, D.H. Polonis, INTERMEDIATE COMPOUNDS Ni8Nb (Cb) IN NICKEL-RICH NICKEL–NIOBIUM (COLUMBIUM) ALLOYS, Trans. Met. Soc. AIME. 245 (1969) 345–349.
[78] L.A. Pantelejmonov, L.V. Aleshina, Investigation of Fe 2 Nb-Ni 3 Nb system alloys, Vestn. Mosk. Univ., Ser. II. Khim. 16 (1975) 630.
[79] K.V. Varli, T.I. Druzhinina, N.P. D'yakonova, S.E. Pirogova, A.M. Rutman, Effect of cobalt and nickel alloying on stability of phases of Fe-Nb system, Izv. Vyss. Uchebn. Zaved., Chern. Met. 9 (1981).
[80] Y.A. Skakov, N.P. D'yakonova, V.V. Savin, V.K. Semina, A.V. Sharshatkina, Cooling rate effect on phase structure for Fe-Co-Nb and Fe-Ni-Nb melts, Izv. Vyss. Uchebnykh Zaved. Chernaya Metall. (1984) 85–90.
[81] V.V. Savin, Formation and stability of Laves phases in the system Ni-Fe-Nb, Fiz. Met. i Metalloved. Akad. Nauk SSSR, Ural. Fil. 68 (1989).
[82] T. Ueyama, M.M. Ghanem, N. Miura, M. Takeyama, T. Matsuo, in: Phase Stability of Ni 3 Nb-δ Phase in Ni-Nb-M Systems at Elevated Temperatures, in: THERMEC97, Intern. Conf. Thermomechan. Proc. Steels Other Mater, TMS, Warrendale, USA, 1997, pp. 1753–1760.
[83] M. Takeyama, S. Morita, A. Yamauchi, M. Yamanaka, T. Matsuo, E.A. Loria, Superalloys 718, 625, 706 and Various Derivatives, By EA Loria, TMS 333 (2001).
[84] J.C. Zhao, M.R. Jackson, L.A. Peluso, L.N. Brewer, A diffusion-multiple approach for mapping phase diagrams, hardness, and elastic modulus, Jom 54 (2002) 42–45, https://doi.org/10.1007/BF02700985.
[85] J.C. Zhao, Combinatorial approaches as effective tools in the study of phase diagrams and composition-structure-property relationships, Prog. Mater. Sci. 51 (2006) 557–631, https://doi.org/10.1016/j.pmatsci.2005.10.001.
[86] J.C. Zhao, M.R. Jackson, L.A. Peluso, Determination of the Nb-Cr-Si phase diagram using diffusion multiples, Acta Mater 51 (2003) 6395–6405, https://doi.org/10.1016/j.actamat.2003.08.007.
[87] S. Cao, J.C. Zhao, Application of dual-anneal diffusion multiples to the effective study of phase diagrams and phase transformations in the Fe-Cr-Ni system, Acta Mater 88 (2015) 196–206, https://doi.org/10.1016/j.actamat.2014.12.027.
[88] J.C. Zhao, High-Throughput and Systematic Study of Phase Transformations and Metastability Using Dual-Anneal Diffusion Multiples, Metall. Mater. Trans. A Phys. Metall. Mater. Sci. 51 (2020) 5006–5022, https://doi.org/10.1007/s11661-020-05915-w.
[89] J. Zhao, Diffusion Multiples, Methods Phase Diagr. Determ. (2007) 246–272.

[90] S.L. Shang, Y. Wang, D. Kim, Z.K. Liu, First-principles thermodynamics from phonon and Debye model: Application to Ni and Ni3Al, Comput. Mater. Sci. 47 (2010) 1040–1048.
[91] Y. Wang, Z.K. Liu, L.Q. Chen, Thermodynamic properties of Al, Ni, NiAl, and Ni3Al from first-principles calculations, Acta Mater 52 (2004) 2665–2671, https://doi.org/10.1016/j.actamat.2004.02.014.
[92] G. Kresse, J. Furthmüller, Efficient iterative schemes for ab initio total-energy calculations using a plane-wave basis set, Phys. Rev. B. 54 (1996) 11169.
[93] P.E. Blöchl, Projector augmented-wave method, Phys. Rev. B. 50 (1994) 17953–17979, https://doi.org/10.1103/PhysRevB.50.17953.
[94] J.P. Perdew, K. Burke, M. Ernzerhof, Generalized gradient approximation made simple, Phys. Rev. Lett. 77 (1996) 3865.
[95] C. Wang, W. Zhong, J.C. Zhao, Insights on phase formation from thermodynamic calculations and machine learning of 2436 experimentally measured high entropy alloys, J. Alloys Compd. 915 (2022) 165173, https://doi.org/10.1016/j.jallcom.2022.165173.
[96] K. Choudhary, B. DeCost, Atomistic Line Graph Neural Network for improved materials property predictions, Npj Comput. Mater. 7 (2021) 1–8, https://doi.org/10.1038/s41524-021-00650-1.
[97] A.M. Krajewski, J.W. Siegel, J. Xu, Z.K. Liu, Extensible Structure-Informed Prediction of Formation Energy with improved accuracy and usability employing neural networks, Comput. Mater. Sci. 208 (2022) 111254, https://doi.org/10.1016/j.commatsci.2022.111254.
[98] J.E. Saal, S. Kirklin, M. Aykol, B. Meredig, C. Wolverton, Materials design and discovery with high-throughput density functional theory: The open quantum materials database (OQMD), Jom 65 (2013) 1501–1509, https://doi.org/10.1007/s11837-013-0755-4.
[99] K. Choudhary, K.F. Garrity, A.C.E. Reid, B. DeCost, A.J. Biacchi, A.R. Hight Walker, Z. Trautt, J. Hattrick-Simpers, A.G. Kusne, A. Centrone, A. Davydov, J. Jiang, R. Pachter, G. Cheon, E. Reed, A. Agrawal, X. Qian, V. Sharma, H. Zhuang, S.V. Kalinin, B.G. Sumpter, G. Pilania, P. Acar, S. Mandal, K. Haule, D. Vanderbilt, K. Rabe, F. Tavazza, The joint automated repository for various integrated simulations (JARVIS) for data-driven materials design, Npj Comput. Mater. 6 (2020), https://doi.org/10.1038/s41524-020-00440-1.
[100] M. Hillert, The compound energy formalism, J. Alloys Compd. 320 (2001) 161–176.
[101] O. Redlich, A.T. Kister, Algebraic representation of thermodynamic properties and the classification of solutions, Ind. Eng. Chem. 40 (1948) 345–348.
[102] I. Ansara, N. Dupin, B. Sundman, Reply to the paper:"When is a compound energy not a compound energy? A critique of the 2-sublattice order/disorder model": Of Nigel Saunders, Calphad 20 (1996) 491–499, Calphad 21 (1997) 535–542.
[103] R. Otis, Z.K. Liu, pycalphad: CALPHAD-based Computational Thermodynamics in Python, J. Open Res. Softw. 5 (2017) 1–11, https://doi.org/10.5334/jors.140.
[104] PyCalphad: Python library for computational thermodynamics using the CALPHAD method, Https://Pycalphad.Org. (n.d.).
[105] T. Abe, B. Sundman, A description of the effect of short range ordering in the compound energy formalism, Calphad Comput. Coupling Phase Diagrams Thermochem. 27 (2003) 403–408, https://doi.org/10.1016/j.calphad.2004.01.005.
[106] Z.K. Liu, Theory of cross phenomena and their coefficients beyond Onsager theorem, Mater. Res. Lett. 10 (2022) 393–439, https://doi.org/10.1080/21663831.2022.2054668.
[107] Z.K. Liu, Y. Wang, S.L. Shang, Zentropy Theory for Positive and Negative Thermal Expansion, J. Phase Equilibria Diffus. 43 (2022) 598–605, https://doi.org/10.1007/s11669-022-00942-z.
[108] Z.K. Liu, Thermodynamics and its prediction and CALPHAD modeling: Review, state of the art, and perspectives, Calphad Comput. Coupling Phase Diagrams Thermochem. 82 (2023) 102580, https://doi.org/10.1016/j.calphad.2023.102580.
[109] J.F. Zhao, H.P. Wang, B. Wei, A new thermodynamically stable Nb2Ni intermetallic compound phase revealed by peritectoid transition within binary Nb-Ni alloy system, J. Mater. Sci. Technol. 100 (2022) 246–253, https://doi.org/10.1016/j.jmst.2021.07.001.
[110] Y. Hasebe, K. Hashimoto, M. Takeyama, Phase equilibria among γ-Fe/Fe2Nb (TCP)/Ni3Nb (GCP) phases in Fe-Ni-Nb ternary system at elevated temperatures, J. Japan Inst. Met. 75 (2011) 265–273, https://doi.org/10.2320/jinstmet.75.265.
[111] B. Bocklund, R. Otis, A. Egorov, A. Obaied, I. Roslyakova, Z.K. Liu, ESPEI for efficient thermodynamic database development, modification, and uncertainty quantification: Application to Cu-Mg, MRS Commun 9 (2019) 618–627, https://doi.org/10.1557/mrc.2019.59.
[112] ESPEI: Extensible Self-optimizing Phase Equilibria Infrastructure, Https://Espei.Org. (n.d.).
[113] D. Foreman-Mackey, D.W. Hogg, D. Lang, J. Goodman, emcee : The MCMC Hammer, Publ. Astron. Soc. Pacific. 125 (2013) 306–312, https://doi.org/10.1086/670067.
[114] J. Goodman, J. Weare, Ensemble samplers with affine invariance, Commun. Appl. Math. Comput. Sci. 5 (2010) 65–80, https://doi.org/10.2140/camcos.2010.5.65.
[115] B.B.P. Carlin, T.A. Louis, J. Book Reviews, Am. Stat. Assoc. 109 (2014) 1325–1337, https://doi.org/10.1080/01621459.2014.963405.
[116] J.O. Andersson, T. Helander, L. Höglund, P. Shi, B. Sundman, Thermo-Calc & DICTRA, computational tools for materials science, Calphad Comput. Coupling Phase Diagrams Thermochem. 26 (2002) 273–312, https://doi.org/10.1016/S0364-5916(02)00037-8.
[117] T. Ohba, Y. Kitano, Y. Komura, The charge-density study of the Laves phases, MgZn2 and MgCu2, Acta Crystallogr. Sect. C Cryst. Struct. Commun. 40 (1984) 1–5, https://doi.org/10.1107/s0108270184002791.
[118] I.J. Duerden, W. Hume-Rothery, The equilibrium diagram of the system niobium-nickel, J. Less Common Met. 11 (1966) 381–387.
[119] C.J. van der Wekken, R. Taggart, D.H. Polonis, Short-Range Order and the Nucleation of Long-Range Order in Ni-Rich Nickel-Niobium Alloys, Met. Sci. J. 5 (1971) 219–223.